

# Untersuchung der phasengemittelten Motoreinströmung in MR-Umgebung mit Hilfe von MRV

Investigation of the phase-averaged in-cylinder flow in MR environment using MRV

Master-Thesis von Akhil Varma

Matrikelnummer 2713748

Tag der Einreichung:



TECHNISCHE  
UNIVERSITÄT  
DARMSTADT



Center of  
Smart Interfaces

---

## Erklärung

---

Hiermit versichere ich, Akhil Varma, die vorliegende Master-Thesis ohne Hilfe Dritter und nur mit den angegebenen Quellen und Hilfsmitteln angefertigt zu haben. Alle Stellen, die Quellen entnommen wurden, sind als solche kenntlich gemacht worden. Diese Arbeit hat in gleicher oder ähnlicher Form noch keiner Prüfungsbehörde vorgelegen. In der abgegebenen Thesis stimmen die schriftliche und elektronische Fassung überein.

---

Ort, Datum

---

Unterschrift (Akhil Varma)

Inhaltsverzeichnis	II
Nomenklatur	IV
Abbildungsverzeichnis	VI
Tabellenverzeichnis	VIII
1 Motivation	1
2 Magnetic Resonance Velocimetry: The Theory	2
2.1 Magnetic Resonance Imaging	2
2.1.1 Spin precession	2
2.1.2 Magnetic resonance	2
2.1.3 Spin echo relaxation	3
2.1.4 Slice selection	4
2.1.5 Obtaining the MR image	4
2.2 Advantages and Disadvantages of MRV	4
3 Magnetic Resonance Velocimetry: The Experiments	6
3.1 Model engine	6
3.2 Valve timing for model engine	7
3.3 Volume influx for model engine	9
3.4 Comparison of Reynolds numbers	10
3.5 Experimental setup	11
3.6 MR pulse sequence and measurement	11
3.7 Preliminary results and Post-processing	12
3.7.1 Signal to noise ratio (SNR) and artefacts	13
3.7.2 Removal of artefacts and image correction using Legendre polynomials	13
3.7.3 Ist vs Soll	13
4 Validation of MRV data with PIV data	15
4.1 Basis for comparison of MRV data with PIV data	15
4.1.1 Normalization of the velocity fields	15
4.1.2 Scaling factor	16
4.2 Methods of comparison of MRV and PIV data	16
4.2.1 Qualitative comparison using Correlation Coefficients	17
4.2.2 Quantitative comparison using Root Mean Square Deviation (RMSD)	18
4.2.3 Predicting the region of validity	18
4.2.4 Effects of Compressibility	19
5 Flow through the valve curtain	20
5.1 Coordinate system definition	20
5.2 Evolution of flow through the valve curtain during the intake stroke	20
5.2.1 Recirculation of flows	21
5.2.2 Stage 1: Opening and closing stages of the valves	22
5.2.3 Stage 2: Uniform outflow ( $-343^\circ \text{ bTDC} \leq \alpha \leq -306^\circ \text{ bTDC}$ )	22
5.2.4 Stage 3: Growth of Recirculation region ( $-297^\circ \text{ bTDC} \leq \alpha \leq -270^\circ \text{ bTDC}$ )	24
5.2.5 Stage 4: Stagnation of Recirculation region ( $-260^\circ \text{ bTDC} \leq \alpha \leq -222^\circ \text{ bTDC}$ )	25
5.2.6 Stage 5: Decay of Recirculation region ( $-213^\circ \text{ bTDC} \leq \alpha \leq -185^\circ \text{ bTDC}$ )	27
5.2.7 Stage 6: Re-formation of uniform flow region ( $-176^\circ \text{ bTDC} \leq \alpha \leq -148^\circ \text{ bTDC}$ )	29

---

6	Analysis of vortex structures from MRV data	30
6.1	Identification of vortex cores . . . . .	30
6.1.1	The Q-criteria . . . . .	30
6.1.2	Kinematic vorticity number, $N_k$ . . . . .	30
6.2	Major vortex cores that have been identified from MRV data . . . . .	31
6.2.1	Toroid vortices . . . . .	31
6.2.2	Horse-Shoe vortices . . . . .	33
6.2.3	Valve stem vortices . . . . .	33
6.3	Kinematic vorticity number . . . . .	33
6.4	Measuring region of influence of the vortices . . . . .	33
6.4.1	Toroid vortices . . . . .	34
6.4.2	Horse-shoe vortices . . . . .	34
6.4.3	Valve-stem vortices . . . . .	34
	Anhang	IX
	Literaturverzeichnis	IX



---

## Symbolverzeichnis

---

### Abkürzungen

$\alpha$	Crank angle [ $rad$ ]
$\dot{V}$	Volume flux [ $m^3 s^{-1}$ ]
$\eta$	coordinate axis along valve stem axis [ ]
$\gamma$	Gyromagnetic ratio [ $rad s^{-1} T^{-1}$ ]
$\gamma_{XY}$	Pearson's correlation coefficient [ ]
$\gamma_D$	Directional correlation coefficient [ ]
$\nu_a$	Kinematic viscosity of air [ $m^2 s^{-1}$ ]
$\nu_w$	Kinematic viscosity of water [ $m^2 s^{-1}$ ]
$\omega_c$	Angular velocity of crank [ $rad s^{-1}$ ]
$\Omega_{ij}$	Rotation rate tensor [ $s^{-1}$ ]
$\S_{ij}$	Strain rate tensor [ $s^{-1}$ ]
$\theta$	Angle around the valve [ $rad$ ]
$B$	Magnetic field strength [ $T$ ]
$D$	Diameter of the piston [ $m$ ]
$d$	Diameter of the cross-section at which Reynolds number is calculated [ $m$ ]
$G_{ij}$	Velocity gradient tensor [ $s^{-1}$ ]
$l_c$	Length of connecting rod [ $m$ ]
$M$	Mach number [ ]
$MRV$	Magnetic resonance velocimetry [ ]
$n$	Oscillation frequency of valves [ $s^{-1}$ ]
$N_k$	Kinematic vorticity number [ ]
$NF$	Normalization factor [ $m s^{-1}$ ]
$PIV$	Particle Image Velocimetry [ ]
$PWM$	Pulse width modulation [ ]
$Q$	Second invariant of velocity gradient [ ]
$r_c$	Crank radius [ $m$ ]
$Re$	Reynolds number [ ]
$Re_o$	Reynolds number associated with oscillating bodies
$RF$	Radio frequency [ ]
$RMSD$	Root Mean Square Deviation [ $m s^{-1}$ ]

---

---

$SF$	Scaling Factor [ ]
$SNR$	Signal to Noise Ratio []
$St$	Strouhal number []
$T_{model}$	Time period of oscillation of valves of model engine [s]
$T_{real}$	Time period of oscillation of valves of equivalent real engine [s]
$TE$	Echo time [s]
$TR$	Repetition time [s]
$U_m$	Velocity from MRV data [ $m\ s^{-1}$ ]
$U_p$	Velocity from PIV data [ $m\ s^{-1}$ ]
$VENC$	Velocity encoding [ $m/s$ ]

1.1	Optical engine [RSM, TU Darmstadt] . . . . .	1
1.2	Optical engine [Rieß (2014)] . . . . .	1
2.1	Net magnetization due to excess spin [Hendrix (2003)] . . . . .	2
2.2	Precession of the magnetization about the magnetic field [Hendrix (2003)] . . . . .	2
2.3	Flipping of the magnetization by a 90 degree RF pulse[Hendrix (2003)] . . . . .	3
2.4	Free induction decay of the Transverse magnetization[Hendrix (2003)] . . . . .	3
2.5	Selection of slice position by using a gradient magnetic field signal [Hendrix (2003)] . . . . .	4
2.6	Obtaining the MR image from the encoded data in k-space [Hendrix (2003)] . . . . .	4
3.1	Model of the inlet valves . . . . .	6
3.2	Model of the engine and its cross-sectional view in the mid-valve plane . . . . .	6
3.3	Experimental setup with the new engine [Rieß (2014)] . . . . .	7
3.4	Schematic of the IC engine . . . . .	8
3.5	Schematic of the experimental setup . . . . .	11
3.6	A FlowOn raw data obtained from MR scan . . . . .	12
3.7	Blanking of artefacts by chopping off the data in the region . . . . .	13
3.8	Comparison of velocity magnitudes from FlowOff data before and after correction . . . . .	14
3.9	Ist vs Soll of the volume influx . . . . .	14
4.1	Constant X and constant Y grid lines (in mm) . . . . .	15
4.2	Contour plot of Velocity magnitude (in m/s) of MRV(left) and PIV data at crank position $-270^\circ$ bTDC. $Y = -10\text{mm}$ is marked in red dotted line. . . . .	16
4.3	Plot of normalized u and v velocities from Table 4.2 . . . . .	17
4.4	Normalized u velocity at $X=-30\text{ mm}$ ; Crank at $-330^\circ$ bTDC . . . . .	17
4.5	Green sides represent sections where the acceptability condition is met. Red sides represent regions where it is not. Hatched areas represent region of validity. All dimensions are in $\text{mm}$ . . . . .	19
5.1	Valve curtain with iso-surface of radius = $15.5\text{ mm}$ . . . . .	20
5.2	Schematic of flows through valve curtain . . . . .	21
5.3	Percentage recirculation into the valve curtain at various crank positions . . . . .	21
5.4	2D projection of flow through the valve curtain in the opening and closing stages . . . . .	22
5.5	Division of valve curtain into sections. Average percentage flow through each section is also shown. The average percentage per unit $\theta(^{\circ})$ is shown in brackets. . . . .	23
5.6	2D projection of flow through the valve curtain in the uniform flow stage . . . . .	23
5.7	Average percentage outflow through the different sections of the valve during Growth stage. The average percentage per unit $\theta(^{\circ})$ is shown in brackets. . . . .	24
5.8	2D projection of flow through the valve curtain in the growth of recirculation region stage . . . . .	25
5.9	Redirection of streamlines on the valves due to valve stem vortices . . . . .	25
5.10	Average percentage outflow through the different sections of the valve during Stagnation stage. The average percentage per unit $\theta(^{\circ})$ is shown in brackets. . . . .	26
5.11	2D projection of flow through the valve curtain in the Stagnation of recirculation region stage . . . . .	27
5.12	Average percentage outflow through the different sections of the valve during Decay stage. The average percentage per unit $\theta(^{\circ})$ is shown in brackets. . . . .	28
5.13	2D projection of flow through the valve curtain in the decay of recirculation region stage . . . . .	28
5.14	2D projection of flow through the valve curtain in the reformation of uniform flow stage . . . . .	29
6.1	Vortex cores located in mid-valve plane . . . . .	31
6.2	Contour plot of $Q$ at crank angle $-250^\circ$ bTDC representing the closed core of Toroid vortices at different XZ-planes . . . . .	32
6.3	Iso-surface of $Q = 0.05$ at crank angle $-269^\circ$ bTDC representing the core of Toroid vortices when viewed from the bottom of the engine cylinder. Vorticity magnitude is shown in $\text{sec}^{-1}$ . . . . .	32
6.4	Iso-surface of $Q = 0.1$ at crank angle $-232^\circ$ bTDC representing the core of Horse-shoe vortex . Vorticity magnitude is shown in $\text{sec}^{-1}$ . . . . .	33

---

6.5	Iso-surface of $Q = 0.1$ at crank angle $-250^\circ$ bTDC representing the core of valve stem vortex . Vorticity magnitude is shown in $\text{sec}^{-1}$ . . . . .	34
6.6	Contour plot of $Q$ at crank angle $-250^\circ$ bTDC representing the core of valve stem vortex. . . . .	34

---

## Tabellenverzeichnis

---

3.1	Kinematic viscosities of water and air at different temperatures . . . . .	9
4.1	u and v velocity components of sample MRV and PIV data . . . . .	16
4.2	Normalized u and v velocity components of sample MRV and PIV data . . . . .	16
4.3	Comparison of correlation coefficients . . . . .	18
5.1	Stages of evolution of flow through the valve curtain . . . . .	21
5.2	%Recirculation behind the valve at different crank position . . . . .	24
5.3	Percentage recirculation behind the valve at various crank angles . . . . .	26
5.4	Percentage recirculation behind the valve at various crank angles . . . . .	27

---

## 1 Motivation

---

A current research project at the department of Reactive flows and Diagnostics (RSM) at Technische Universitat Darmstadt is the investigation of the in-cylinder flow inside a single cylinder 4 stroke diesel engine with optical access from various positions that allow the study of flow with optical measurement techniques like PIV, Tomo-PIV etc.. while the engine is running. A model of the engine is shown in Figure 1.1.

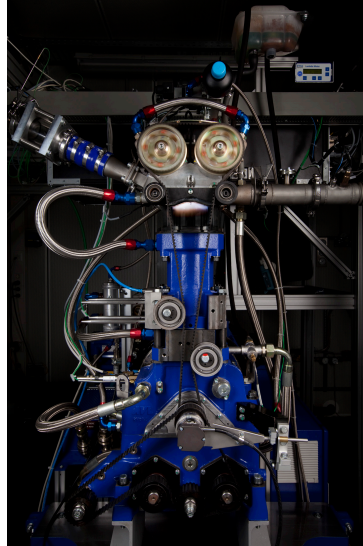


Abbildung 1.1: Optical engine [RSM, TU Darmstadt]

But no flow data can be obtained inside the intake-channel and in direct proximity of the intake valves due to missing optical access. However, the flow phenomena in these regions during the intake-suction stroke can have great influence on the overall engine performance.

The department Center of Smart Interfaces (CSI) at Technische Universitat Darmstadt conducts flow measurements using a MRI scanner in cooperation with the Department of Radiology at the University hospital, Freiburg. This technique for measuring the three-dimensional velocity fields is called Magnetic Resonance Velocimetry (MRV). MRV uses the principle of Magnetic Resonance Imaging to provide flow data without the need for optical access.

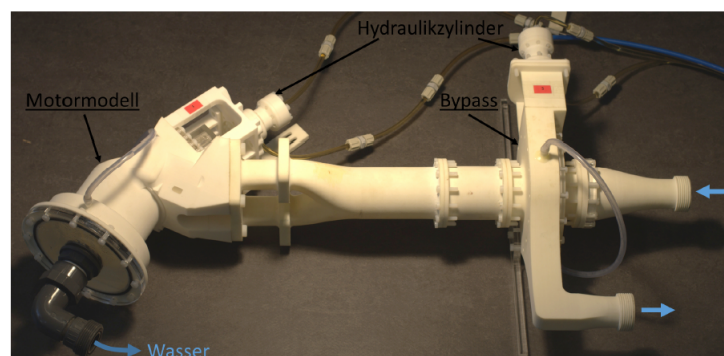


Abbildung 1.2: Optical engine [Rieß (2014)]

It is a relatively new measurement technique being used for engineering applications. MRV data of a first model of the engine (Shown in Figure 1.2 ) with fixed valve lift showed excellent comparison with in-cylinder PIV data. The next iteration of the project involved equipping the model with movable valves and controllable intake .Using this model engine, the MRV experiments can be carried out to measure the inflow during the entire intake stroke of the engine.

---

## 2 Magnetic Resonance Velocimetry: The Theory

---

### 2.1 Magnetic Resonance Imaging

---

A nucleus with a spin is always magnetic. The smallest volume element that collectively forms the entire region of measurement is known as a "voxel". Inside the voxel of a material with a non-zero magnetic spin, the direction of magnetic spin of the nuclei point randomly in all directions and hence, the ensemble magnetic spin is zero. When the test section is moved into a strong magnetic field ( $\vec{B}$ ), the spin of the nuclei align themselves in the direction of the magnetic field. They can align parallel or anti-parallel to the field.[Hendrix (2003)] Due to excess spins, the ensemble

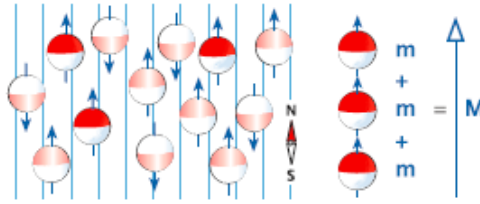


Abbildung 2.1: Net magnetization due to excess spin [Hendrix (2003)]

has a net non-zero magnetization ( $\vec{M}$ ). The value of  $M$  grows with increase in proton density, increase in strength of external magnetic field ( $\vec{B}$ ), and decrease in temperature.

---

#### 2.1.1 Spin precession

---

Spin magnets have a unique characteristic that they can precess about the direction of magnetic field. The frequency of precession, known as the "Larmor frequency" is given by

$$\vec{\omega} = \gamma \times \vec{B} \quad (2.1)$$

where,  $\gamma$  is the gyromagnetic ratio of the nucleus.

For a 1 T external magnetic field, the Larmor frequency for a proton lies in the range of radio waves. [Hendrix (2003)]

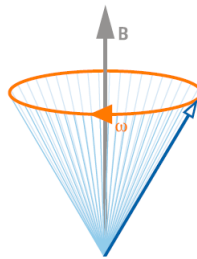


Abbildung 2.2: Precession of the magnetization about the magnetic field [Hendrix (2003)]

---

#### 2.1.2 Magnetic resonance

---

When an external pulse having the same frequency as that of the precession frequency is made to interfere, the magnetization will flip or tilt depending on the strength of the pulse. Since the precession frequency falls in the RF range, an RF pulse is used. The angle by which it tilts is called the "tilt angle/flip angle" ( $\phi$ ). For example, a  $90^\circ$  RF pulse will flip the magnetization by 90 degrees.

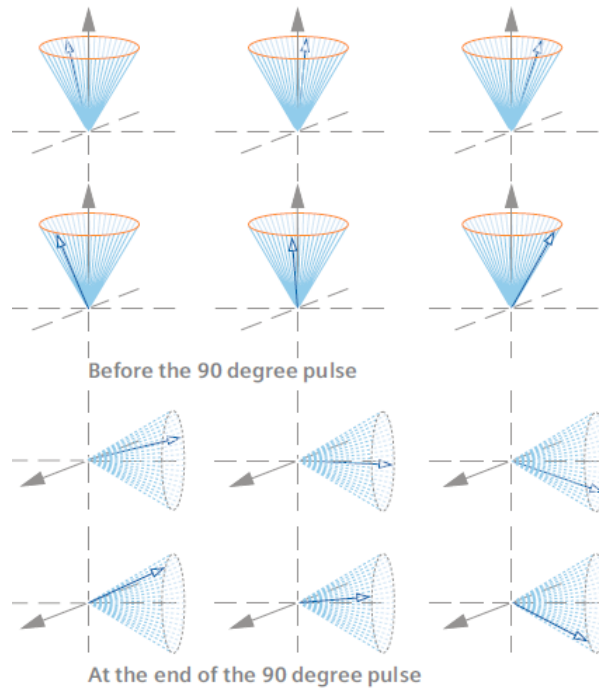


Abbildung 2.3: Flipping of the magnetization by a 90 degree RF pulse[Hendrix (2003)]

The ensemble longitudinal magnetization effectively cancels out after the flip. Since they precess in-phase after flipping, there occurs a net transverse magnetization of the same strength as the longitudinal magnetization. Once the RF pulse is removed, the transverse magnetization decays as the magnetization re-aligns itself with the external magnetic field  $\vec{B}$ . This is called Free Induction Decay (FID)[Hendrix (2003)]. The recovery of longitudinal

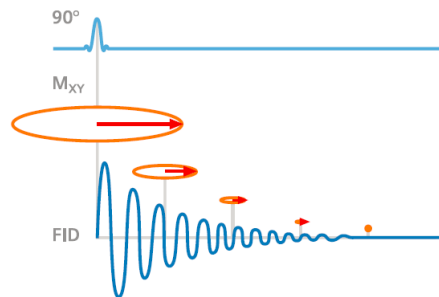


Abbildung 2.4: Free induction decay of the Transverse magnetization[Hendrix (2003)]

magnetization, known as Longitudinal Relaxation, follows an exponential behaviour. The spins become out of phase again.

The decaying transverse magnetic field can induce current in a MR coil. This is the MR signal that is received. For a given strength of external magnetic field and RF signal, the strength of MR signal depends on the proton density.

### 2.1.3 Spin echo relaxation

As the process of FID is very fast, all the data cannot be captured as quickly. This problem is overcome by a principle called "spin-echo relaxation"[Hendrix (2003)]. When a  $180^\circ$  pulse is given to the nuclei before total decay, the spins get flipped, while the direction of rotation remains the same and thus, they align together once again, giving the old data back (known as "echo")



---

#### 2.1.4 Slice selection

---

A slice is a set of voxels along one direction in space. To analyse a particular slice in space, a gradient magnetic field is used. A RF pulse would excite the most nuclei under the influence of a magnetic field of strength  $\frac{RF}{\gamma}$ . So, a particular region in the gradient field having strength equal to or close to this value gives a relatively stronger MR signal compared to the other regions in space.

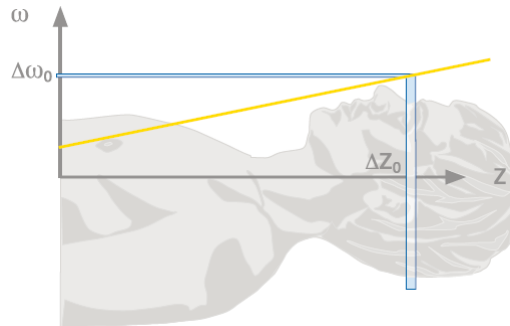


Abbildung 2.5: Selection of slice position by using a gradient magnetic field signal [Hendrix (2003)]

---

#### 2.1.5 Obtaining the MR image

---

The frequency and phase encoded data of the entire set of voxels is known as k-space. A 2D Fourier transform of this k-space gives the raw data values of magnitude and phase of signals of each frequency, from which velocity fields are reconstructed. This reconstruction requires encoding the maximum velocity (VENC) expected in the flow field to get

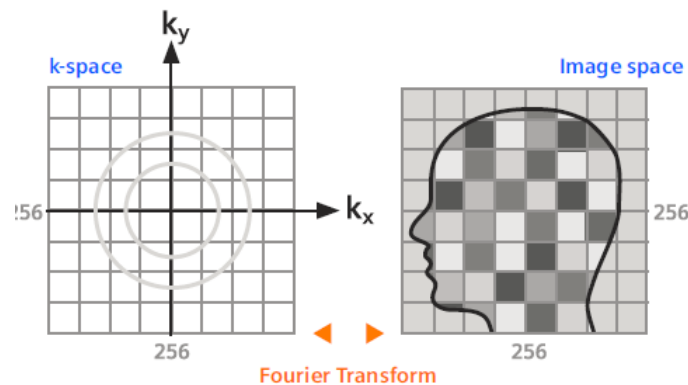


Abbildung 2.6: Obtaining the MR image from the encoded data in k-space [Hendrix (2003)]

the actual flow field. VENC is usually kept 1.5 times the maximum expected velocity.

---

## 2.2 Advantages and Disadvantages of MRV

---

The main advantages of using MRV technique are [Elkin u. Alley (2007)]

1. It is non-invasive: Since no physical device is needed to probe for the velocity, it does not affect the flow in any manner.
2. It does not require optical access: Since MR signal can penetrate through solid surfaces, an optical access is not required to observe the flow. For this reason, flow through any complex geometry can be analysed.
3. It can give phase averaged 3D velocity field over time
4. Because of advancements in rapid prototyping techniques like 3D printing and LASER cutting, any complex MR compatible flow geometries and models can be manufactured easily.

---

Even though the advantages seem promising, there are some disadvantages associated with MRV technique:

1. Flow geometries and models should not be made of materials sensitive to magnetic field like iron or steel.
2. The operating fluid must be sensitive to magnetic field. This requires the molecules of the fluid to have sufficient number of protons. So, fluids like water can be used where as air cannot. This implies that compressible flows are difficult to be analysed using MRV.
3. MRV gives phase averaged data. This means that data regarding instantaneous flow fields are not available. Thus, turbulence measurements are difficult to be obtained from just MRV data.
4. MR imaging requires selection of the right sequence and optimum flip angles. Slight errors will give rise to formation of ghosting effects and artefacts which will reduce the signal to noise ratio (SNR) and will distort the obtained data.
5. Requires an estimate of the maximum flow velocities to calculate the VENC.

A detailed review of the applications, advantages or disadvantages and precautions while using MRV is made in Elkin u. Alley (2007).

It has been observed that the use of MRV for measurement of unsteady flow fields compared to the analytical predictions are also very accurate [Frayne u. a. (1995)]. This allows the use of MRV for analysing unsteady flows inside an IC engine.

---

### 3 Magnetic Resonance Velocimetry: The Experiments

---

The objective is to analyse the flow near the valves of an IC engine using the principle of MR mentioned in chapter 1. Since there is no optical access for the measurement of flows over the valves in the optical engine, PIV measurements cannot be made. Once validated with the PIV measurements inside the engine, the MRV measurements can be used to understand these flows. Similar measurements for stationary valves at  $-270^\circ$  bTDC were made by Freudenhammer u. a. (2014). The same coordinate system will be used for this analysis.

---

#### 3.1 Model engine

---

The model engine was sintered out of polyamide resin ,which is insensitive to magnetic field, using LASER sintering technique. It is a 1:1 scale model of a 500cc, spray guided engine having bore diameter of 86 mm and a stroke of 86mm. The intake valves have a diameter of 31mm and a maximum displacement of 9.5 mm along its axis.



Abbildung 3.1: Model of the inlet valves

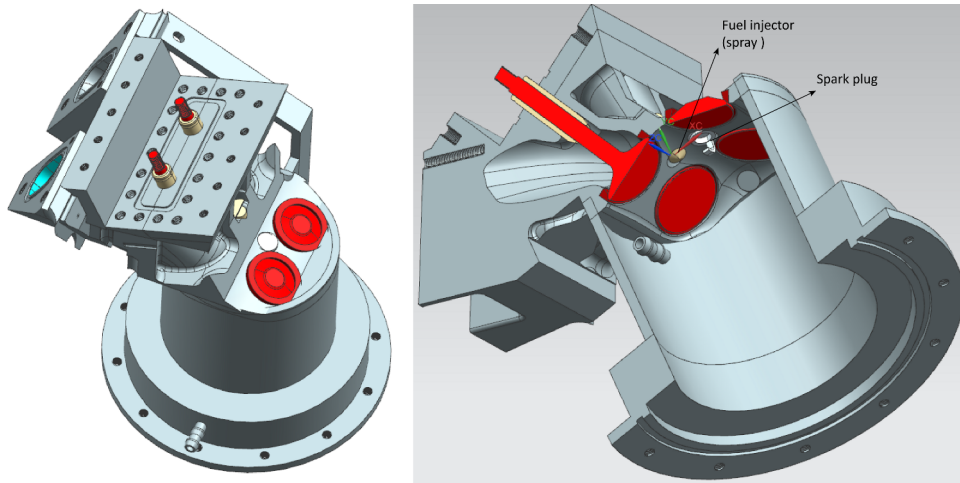


Abbildung 3.2: Model of the engine and its cross-sectional view in the mid-valve plane

The exhaust valves of the model engine are made fixed to the cylinder. The model engine is as shown in Figure 3.2. It was designed in Siemens NX software.

The model engine does not have a piston. To account for its effect, a bypass valve is made at the entry to control the inflow, in accordance with the theoretical intake due to the piston. It consists of a rotor and a stator. The rotor is actuated hydraulically by an oil powered bypass actuation cylinder, controlled automatically using LABVIEW ,Arduino UNO and the hydraulic system as shown in Figure 3.3. Further details regarding the experimental set up and control of the bypass and the valves is available in Rieß (2014). When the valves are fully closed, the bypass is also fully closed and the flow is redirected radially outwards and into the water tank. When fully open, the entire flow is directed towards the engine cylinder through the inlet port. The flow is made to pass through a flow straightener (Honeycomb structure) to minimize the lateral velocity caused by swirling during entry.

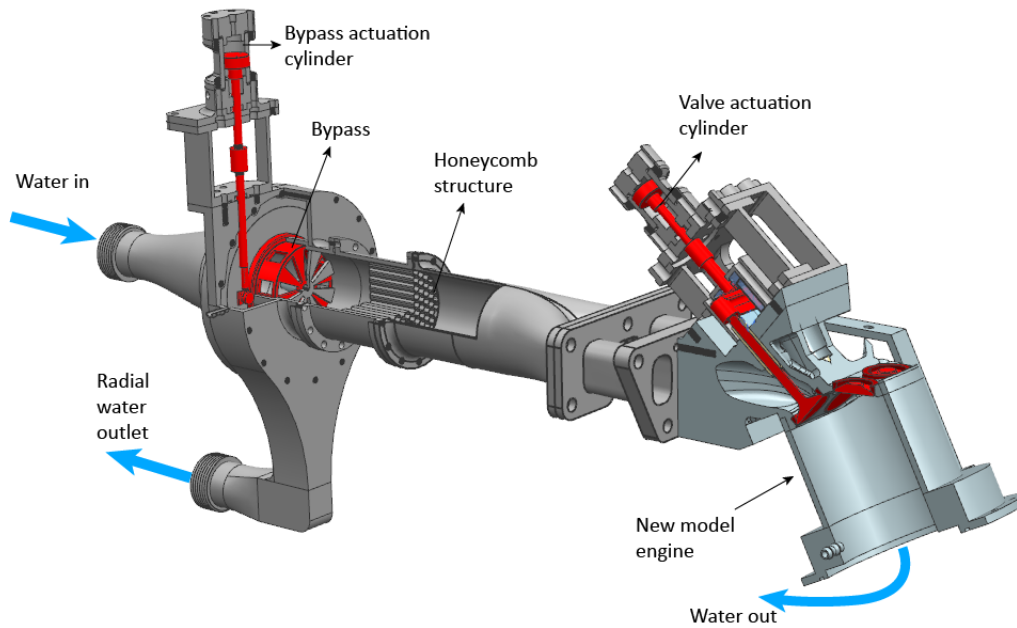


Abbildung 3.3: Experimental setup with the new engine [Rieß (2014)]

The flow splits and flows through the two inlet ports, over the valves and into the cylinder. The water in the cylinder is drawn out by the motor, back into the water tank.

---

### 3.2 Valve timing for model engine

---

#### Assumptions

1. The instantaneous volume flux of air entering the engine cylinder during the suction stroke is assumed to be same as the volume displaced by the piston at that instant.

The following parameters are defined for a real engine

1. Radius of crank =  $r_c = 0,043 \text{ m}$
  2. Length of connecting rod =  $l_c = 0,148 \text{ m}$
  3. Angular velocity of crank =  $\omega_c$
  4. Displacement velocity of piston =  $\dot{x}$
  5. Diameter of the piston (or cylinder) =  $D = 0,086 \text{ m}$
  6. Diameter of the cross-section at which Reynolds number is calculated =  $d = 0,05633 \text{ m}$
  7. Kinematic viscosity of air at  $25^\circ\text{C}$  =  $\nu_a = 155,7 \cdot 10^{-7} \text{ m}^2/\text{s}$
-

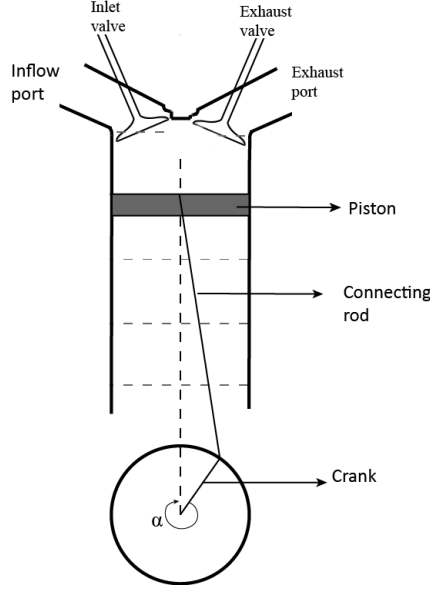


Abbildung 3.4: Schematic of the IC engine

8. Kinematic viscosity of water at  $22^{\circ}\text{C} = \nu_w = 9,2 \cdot 10^{-7} \text{m}^2/\text{s}$

The Strouhal number associated with the flow around an oscillating valve is given by

$$St = \frac{nL}{U} \quad (3.1)$$

where  $n$  is the oscillation frequency;  $L$  is the associated length scale;  $U$  is the flow velocity over the moving valves. In combination with the Reynolds number described in Equation 3.6, we can define a new non dimensional number of the form

$$\frac{nL}{U} \cdot \frac{UL}{\nu} = \frac{nL^2}{\nu} \quad (3.2)$$

This non-dimensional number is the Reynolds number associated with a fluid of viscosity  $\nu$ , flowing over a body having characteristic length  $L$ , and oscillating with  $n$  rev/unit time is given by

$$Re_o = \frac{nL^2}{\nu}$$

This number is used in flows over bodies exhibiting oscillatory motion which is common in biological locomotion [Taylor (1951)]. For similarity of flows over the oscillating valves, this non-dimensional number has to be the same for the real engine and the model engine. Since it is a 1:1 scale model, the length scale ( $L$ ) associated with the valves are same for both the real engine and the model.

$$(Re_o)_{real} = (Re_o)_{model}$$

$$\frac{n_{real}}{\nu_a} = \frac{n_{model}}{\nu_w}$$

which implies,

$$\nu_a \cdot T_{real} = \nu_w \cdot T_{model}$$

or, cycle time of valves of the model engine (in minutes)

$$T_{model} = \frac{\nu_a \cdot T_{real}}{\nu_w} \quad (3.3)$$

The valves have a cycle between crank angles of  $\alpha = 330^\circ$  to  $\alpha = 600^\circ$  i.e. of  $3\pi/2$  radians. In a real engine, the crank covers  $360^\circ(2\pi \text{ radians})$  in  $1/N_{real}$  min. So, the time taken between opening and closing of valves is  $\frac{3\pi}{2 * 2\pi * N_{real}}$  minutes i.e.

$$T_{real} = \frac{3}{4 * N_{real}}$$

Substituting this in Equation 3.3, the cycle time of valves (in seconds) is

$$T_{model} = \frac{3}{4} * \left(\frac{\nu_a}{\nu_w}\right) * \frac{60}{N_{real}} \quad (3.4)$$

Temperature (in $^\circ\text{C}$ )	Kinematic viscosity of water (in $\times 10^{-8} m^2/s$ )	Kinematic viscosity of air (in $\times 10^{-5} m^2/s$ )
20	1.0047	1.511
22	0.92	1.526
24	0.903	1.541
26	0.873	1.564
28	0.836	1.578
30	0.801	1.591

Tabelle 3.1: Kinematic viscosities of water and air at different temperatures

The results of MRV are better at lower temperatures of water, especially in between  $20^\circ\text{C}$  and  $30^\circ\text{C}$ . The viscosities of water and air are shown in the Table 3.1. If we assume the equivalent real engine to be operating at 800 rpm,

$$T_{model} = \frac{3}{4} * \left(\frac{155,7 \cdot 10^{-7}}{9,2 \cdot 10^{-7}}\right) * \frac{60}{800} = 0.932 \text{ sec}$$

But, due to constraints of the oil pumping motors which move the valves by hydraulic pressure, cycle time of the valves of the model engine cannot be reduced below 1.5 sec.

$$T_{model} \geq 1.5 \text{ sec}$$

So, from Equation 3.4,

$$\frac{3}{4} * \left(\frac{155,7 \cdot 10^{-7}}{9,2 \cdot 10^{-7}}\right) * \frac{60}{N_{real}} \geq 1.5$$

which implies,

$$N_{real} \leq 508 \text{ rpm}$$

The maximum speed of the equivalent real engine for a minimum valve time of 1.5 sec of the model engine operating with  $20^\circ\text{C}$  water is around 500 rpm. Under the same conditions, if we take  $N_{real} = 505 \text{ rpm}$ ,

$$T_{model} \approx 1.508 \text{ sec} \quad (3.5)$$

---

### 3.3 Volume influx for model engine

---

The Reynolds number for a real engine, defined at the location shown in the figure, is given by

$$Re = \frac{U d}{\nu_a} \quad (3.6)$$

where, U is the uniform velocity at the cross-section,

$$U = \frac{\dot{V}}{(\frac{\pi d^2}{4})} = \frac{\dot{x} * (\frac{\pi D^2}{4})}{(\frac{\pi d^2}{4})} = \frac{\dot{x} D^2}{d^2}$$


---

$\dot{V}$  is the volume influx into the engine cylinder. Putting this expression back in (1),

$$Re = \frac{\dot{x} D^2}{\nu_a d} \quad (3.7)$$

From the equations of motion of the piston, the velocity of the piston at any crank angle  $\alpha$  is [Bansal u. Brar (2005)]

$$\dot{x} = \omega \cdot r_c \cdot \left( \frac{(\frac{\lambda}{2}) \sin(2\alpha)}{\sqrt{1 - \lambda^2 \sin^2(\alpha)}} + \sin(\alpha) \right) \quad (3.8)$$

where  $\lambda = \frac{r_c}{l_c} = 0,2905$

The piston has maximum velocity of  $\dot{x}_{max} \approx 1.05 \cdot \omega r_c$

The maximum Reynolds number associated with this velocity of piston is obtained from (2) as

$$Re = \frac{\dot{x}_{max} D^2}{\nu_a d} = \frac{1.05 \cdot \omega r_c D^2}{\nu_a d} = \frac{1.05 \cdot 2\pi N_{real} r_c D^2}{60 \nu_a d}$$

where  $N_{real}$  is the speed of the real engine in rpm. Substituting the known values, the maximum Reynolds number in the real engine is

$$Re_{real} = \frac{6,2 \cdot 10^{-4} \cdot N_{real}}{\nu_a} \quad (3.9)$$

Reynolds number in the model engine having working fluid as water is calculated in the similar manner.

$$Re_{model} = \frac{U d}{\nu_w} = \frac{(\dot{V}_{model}) d}{(\frac{\pi d^2}{4}) \nu_w} = \frac{4 \dot{V}_{model}}{\pi d \nu_w}$$

After substituting the known values, the maximum Reynolds number in the model engine is

$$Re_{model} = 2,46 \cdot 10^7 (\dot{V}_{max})_{model} \quad (3.10)$$

For the flows to be similar in both the real and the model engine, the Reynolds numbers need to be the same.

$$Re_{real} = Re_{model}$$

So, equating (4) and (5), Maximum volume influx for model engine is

$$(\dot{V}_{max})_{model} = 1,618 \cdot 10^{-5} \cdot N_{real} \text{ m}^3/\text{s} = 9,71 \cdot 10^{-2} * N_{real} \text{ L/min}$$

The equivalent real engine speed ( $N_{real}$ ) was taken as 505 rpm to get  $T_{model}$  in Equation 3.5. Substituting the value in the above equation, we get the maximum volume flow rate into the engine cylinder as

$$(\dot{V}_{max})_{model} = 9,71 \cdot 10^{-2} * 505 \approx 49 \text{ L/min} \quad (3.11)$$

---

### 3.4 Comparison of Reynolds numbers

---

Due to the difference in equivalent rpm and the rpm of the real engine, the  $Re$  would be different. From equations and , we get

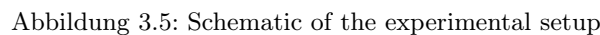
$$Re_{model} \approx 20,000$$

and,

$$Re_{real} \approx 32,000$$

The Reynolds numbers lie in the region  $20,000 < Re < 45,000$ , where the phase averaged flow field remains almost independent of the  $Re$  [Freudenhammer u. a. (2014)]. So, the data can be compared without significant errors.

The experiment was conducted in and with assistance from Radiology lab in Freiburg. It was conducted in 2 separate rooms viz. the control room and the scanning room. As MRI requires the use of strong magnetic fields of the order of 1.5 T to 3 T, objects sensitive to the magnetic field, including metals and all electronic equipments, cannot be placed inside the same scanning room. So, the experiment was controlled remotely from an adjacent control room which is shielded from the strong magnetic field. Only the model engine and the flow tubes were inside the scanning room. Figure 3.5 shows a schematic of the experimental setup.



1. Pump wagon
2. Hydraulic actuation system
3. Temperature controlling unit
4. MR control unit

The servo pumps in the hydraulic actuation system apply hydraulic pressure to actuate the valves. They are controlled by the PWM control signals from Arduino.

The flow rate of water was kept at  $49L/min$  (as obtained in Equation 3.11 of Section 3.3). The hydraulic system was timed to move the valves at  $1.508sec/cycle$ .

The model engine was de-aerated to remove the bubbles before the measurements were taken.

For the MR scanning, a phase contrast imaging(PCI) technique is used. Measurements were taken for 30 phase steps per cycle. The echo time ,  $TE = 3.7ms$  . The repetition time (TR)



between two pulses is equal to the time between each phase step of measurement; which is  $1.508/30 = 0.052\text{sec}$  i.e.  $TR = 52.2\text{ms}$ . The total scanning time was for 51 min 35 sec. For the MR measurements, the expected maximum velocity is of the order of 1m/s. So, a VENC of 1.5 was used. The scanning was performed for the entire 3D space of 256cm x 176cm x 144cm volume over time. Each voxel had the dimensions of 1.6mm x 1.6mm x 1.6mm. 2D measurements over time for the mid-valve, tumble and cross-tumble plane were also conducted. For this data, the spatial and temporal resolution were higher. The spatial resolution was 1mm with measurements at 53 phase steps per cycle.

### 3.7 Preliminary results and Post-processing

The raw data obtained from the experiment is in the form of dicom image files (.dcm). There are 30 phase steps of the MRV data and 192 data sets for each phase step. The MRV data used for analysis is phase averaged from the data sets. A sample image along the cross-tumble plane from Flow-On data is shown in Figure 3.6. These image files are converted into Tecplot readable data files(.dat) after processing it in Velomap 2.54.

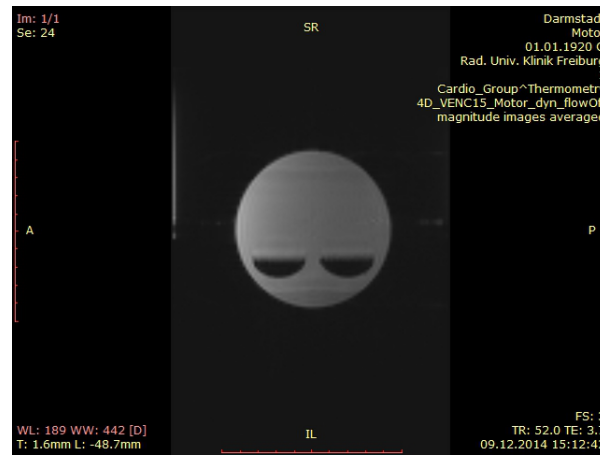


Abbildung 3.6: A FlowOn raw data obtained from MR scan

---

### 3.7.1 Signal to noise ratio (SNR) and artefacts

---

If the VENC value is too low, anti-aliasing occurs and ghosting effects are formed. So, some knowledge of the velocity field is required. Flow related artefacts are formed as a result of object being moved during the scan time. This leads to inter-voxel or intra-voxel dispersion of data. Inconsistencies are formed in the phase encoded direction. If these inconsistencies are periodic, artefacts appear as ghosts of the moving fluid [Hendrix (2004)]. Figure 3.6 also shows an image of these artifacts as the fluid enters the cylinder. For our experiments, the formation of artefacts were minimized by reducing the flip angle.

---

### 3.7.2 Removal of artefacts and image correction using Legendre polynomials

---

The artefacts in the processed Flow-off image files are removed by blanking off the regions where artefacts are presumed to exist (as shown in Figure 3.7) using MATLAB.

This data still contains background noise. For a Flow-off data, the velocity components should have zero value. The original data would show non-zero velocities due to background noise.

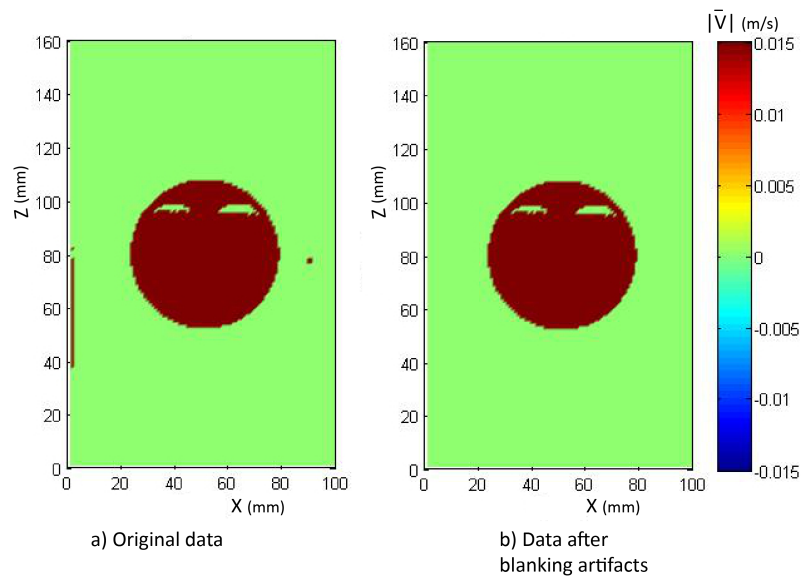


Abbildung 3.7: Blanking of artefacts by chopping off the data in the region

These spatial velocities are first approximated by fitting second order Legendre polynomials to the data. This approximated Flow-off velocity field is subtracted from the original Flow-On data to obtain the corrected flow field.

Actual FlowOn velocity = FlowOn velocity – Approximated FlowOff velocity.

A comparison of the original and the corrected Flow-Off data for U-velocity in the XZ plane is made in Figure 3.8. The corrected files are exported to tecplot readable format and analysed in Tecplot.

---

### 3.7.3 Ist vs Soll

---

Due to the absence of the piston, bypass valves were used for controlling the inflow. To check the validity of behaviour of the inflow, the flow data at the inlet port from the MRV measurements is compared with the expected theoretical inflow due to the piston. The comparison is shown in Figure 3.9. The actual flow rate measured from MRV data is skewed towards the right due to error in Bypass valve timing. But the flow rates lie within the same order of magnitude and show the same trend as that of the theoretical value.

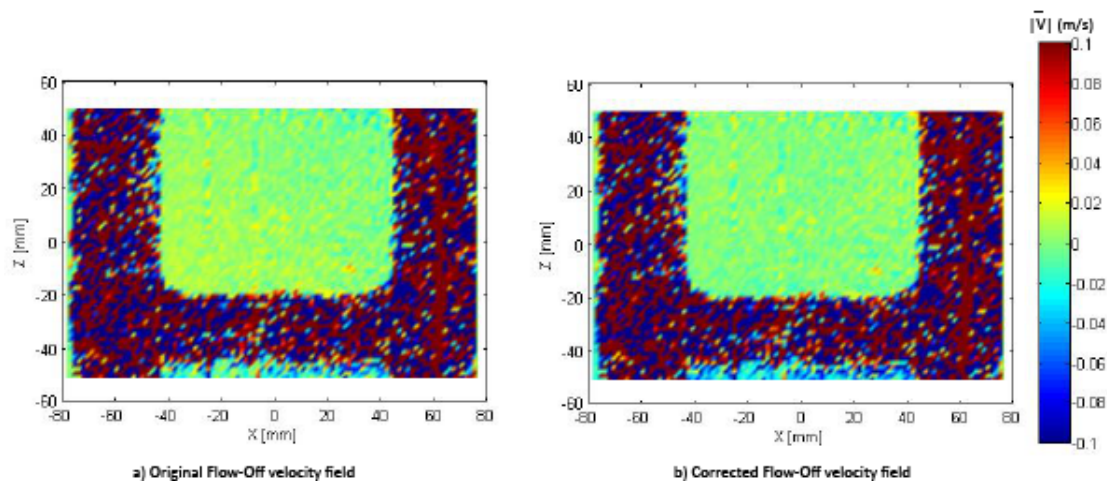


Abbildung 3.8: Comparison of velocity magnitudes from FlowOff data before and after correction

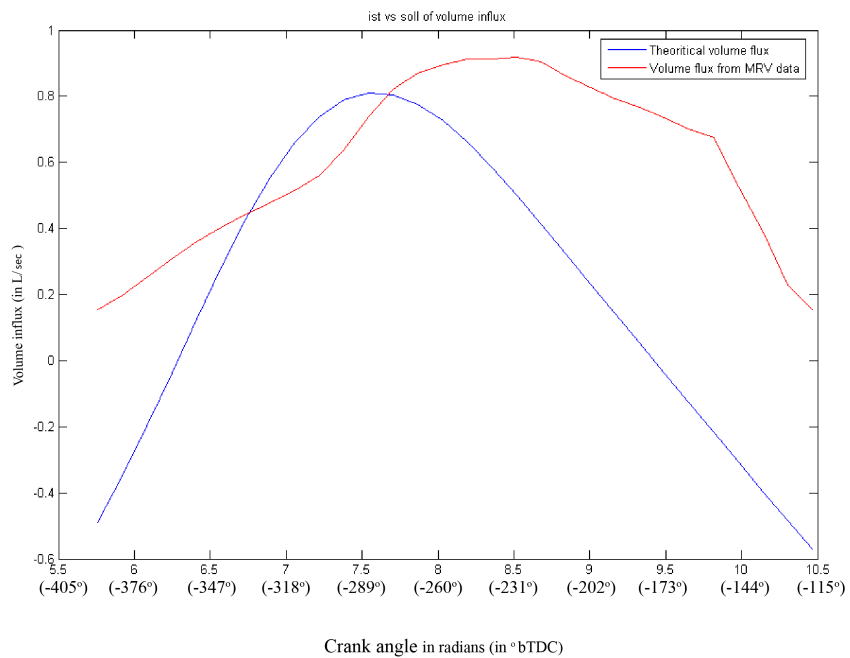


Abbildung 3.9: Ist vs Soll of the volume influx

---

## 4 Validation of MRV data with PIV data

---

### 4.1 Basis for comparison of MRV data with PIV data

---

The MRV measurements give velocity fields. So, a comparison of the velocity fields from MRV with those from PIV, is sufficient to validate it. Freudenhammer u. a. (2014)

For the MRV measurements, water is used as the operating fluid whereas, for the PIV measurements, the fluid is air. As mentioned in Chapter 2, the inflow Reynolds numbers for both the engines are kept as close as possible to one another. So,

$$\frac{U_m}{U_p} \approx \frac{\nu_w}{\nu_a}$$

Since the kinematic viscosity of water at 22°C is much less than that of air at 25°C (approx. 1/17), the average velocities of water in MRV would be scaled by the same order of magnitude to the velocities of air in PIV data. Hence, a direct comparison of the velocity fields is not possible. For bringing the data to a common ground for comparison, the flow fields for both MRV and PIV are normalized.

---

#### 4.1.1 Normalization of the velocity fields

---

The engine geometry in the mid-valve plane is divided into grids as shown in Figure 4.1.

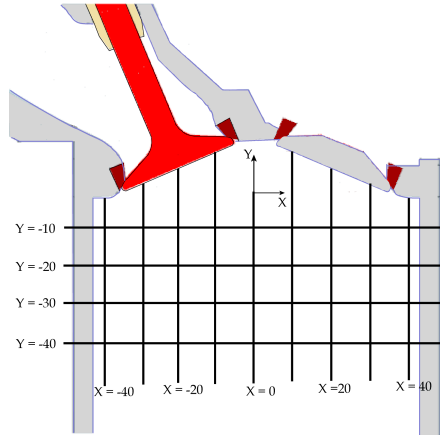


Abbildung 4.1: Constant X and constant Y grid lines (in mm)

The velocity data is normalized along each grid line for both the flow fields and the corresponding data are compared. To normalize the data, a normalization factor, NF, is introduced.

Along any grid line in the x-y plane (mid-valve plane of the engine), the normalization factor is defined as

$$NF = \frac{|u|_{avg} + |v|_{avg}}{2} \quad (4.1)$$

where,  $u_{avg}$  and  $v_{avg}$  represent the average x and y velocity components respectively, along the specified grid. The normalized velocities are defined as

$$\begin{aligned} u_{norm} &= \frac{u}{NF} \\ v_{norm} &= \frac{v}{NF} \end{aligned} \quad (4.2)$$

For brevity, consider an example in which only 1 out of every 10 data points is used to analyse the velocity data from both MRV and PIV (as shown in Figure 4.2) along the line  $Y = -10\text{mm}$ , sampled at every 10mm starting from  $X = -30\text{mm}$  to  $X = 30\text{mm}$ , when the crank is at  $-270^\circ$  bTDC. This data will be used throughout the chapter to give an example of the comparison method.

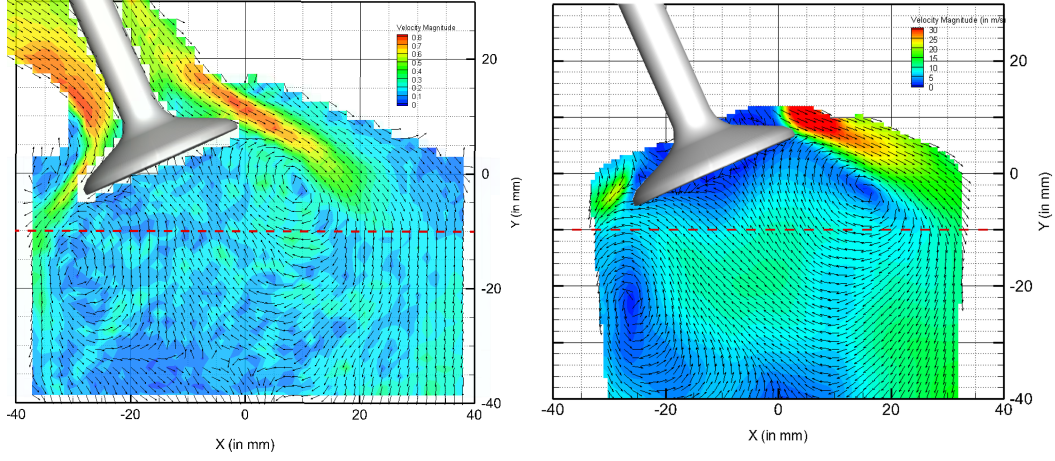


Abbildung 4.2: Contour plot of Velocity magnitude (in m/s) of MRV(left) and PIV data at crank position  $-270^\circ$  bTDC.  $Y = -10\text{mm}$  is marked in red dotted line.

X (in mm)		-30	-20	-10	0	10	20	30
MRV	$u$	-0.102	-0.092	-0.052	-0.31	-0.141	-0.04	-0.002
	$v$	-0.152	0.087	0.076	0.145	0.01	-0.18	-0.157
PIV	$u$	-5.05	-5.374	-4.76	-4.45	-6.208	-6.037	2.82
	$v$	-4.275	4.632	4.809	8.384	5.21	-3.77	-9.844

Tabelle 4.1: u and v velocity components of sample MRV and PIV data

In this case, the  $NF_{\text{MRV}}$  and  $NF_{\text{PIV}}$  are 0.0906 and 5.402 respectively. The normalized velocities found using Equation 4.2 are

X (in mm)		-30	-20	-10	0	10	20	30
MRV	$u_{\text{norm}}$	-1.128	-1.019	-0.569	-0.339	-1.56	-0.439	-0.0273
	$v_{\text{norm}}$	-1.677	0.962	0.841	1.602	0.109	-1.99	-1.738
PIV	$u_{\text{norm}}$	-0.935	-0.995	-0.881	-0.824	-1.149	-1.176	0.5219
	$v_{\text{norm}}$	-0.791	0.858	0.89	1.552	0.964	-0.699	-1.822

Tabelle 4.2: Normalized u and v velocity components of sample MRV and PIV data

In a sense, sum of the normalized velocity components i.e.  $u_{\text{norm}} + v_{\text{norm}}$  is the ratio of the sum of velocity components at every point on the grid line to its mean value.

#### 4.1.2 Scaling factor

The magnitude of velocity from the MRV data can be scaled to the PIV data by using a scaling factor. The scaling factor is defined as the ratio of normalization factors of PIV and MRV.

$$SF = \frac{NF_{\text{PIV}}}{NF_{\text{MRV}}} \quad (4.3)$$

As mentioned in the introduction of this section, the average velocities in MRV and PIV are scaled as the ratios of kinematic viscosities of water and air. The scaling factor (SF), thus, should also be of the same order of magnitude i.e.  $\mathcal{O}(10)$ .

For the above example,  $SF = 59.61$ , which is within the same order of magnitude.

#### 4.2 Methods of comparison of MRV and PIV data

The normalized velocity fields are now the bases for comparison.

A qualitative and quantitative method for the comparison of data is proposed.

The qualitative method is required to compare the flow features. This would verify whether the behaviour of the time averaged flows of MRV is similar to the behaviour of ensemble averaged flows of PIV along a specified line. This, however, would not give a comparison of the magnitude data. A quantitative method is ,thus, required to quantify the deviation in magnitudes of both the normalized data sets.

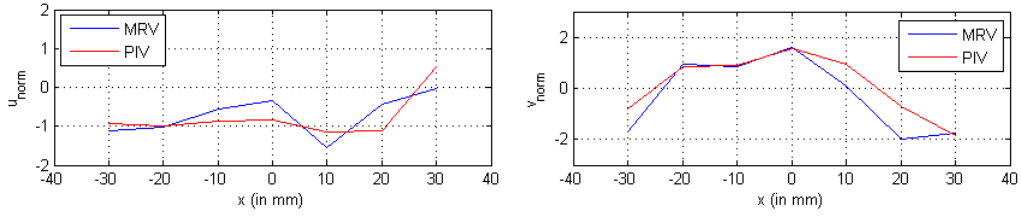


Abbildung 4.3: Plot of normalized u and v velocities from Table 4.2

#### 4.2.1 Qualitative comparison using Correlation Coefficients

A similar trend in both the normalized data sets would imply similar flow behaviour/ features. Comparison of trends in the data are usually done by analysing the correlation between the data using correlation coefficients. The standard method of finding the correlation coefficient between 2 data sets X and Y, is by using Pearson's correlation coefficient [Ross (2010)], which is defined as

$$\gamma_{XY} = \frac{\sum(x_i - \bar{x}) \cdot (y_i - \bar{y})}{\sqrt{\sum(x_i - \bar{x})^2} \cdot \sqrt{\sum(y_i - \bar{y})^2}} \quad (4.4)$$

A perfectly correlated data would have  $\gamma_{XY} = 1$ . An uncorrelated data would have  $\gamma_{XY} = 0$  and a perfectly negatively correlated data would have  $\gamma_{XY} = -1$ .

corrcoef() fuction of MATLAB and CORREL() fuction of Microsoft Excel also give Pearson's correlation coefficient. For the normalized sample data in Table 4.2 (or Figure 4.3), the correlation coefficient of u and v velocities are 0.656 and 0.926 respectively.

#### Need for a Directional Correlation Coefficient

Consider a situation in which the flow behaviour from MRV is exactly the same as that of PIV, but in the opposite direction. This means that the normalized velocities trend in exactly the same manner, but have opposite signs. If only correlation coefficient ( $\gamma_{XY}$ ) is used to compare them in such situations, it would give an erroneous perfect correlation. One such situation is when the piston is close to the valves and the flow reverses after impinging on the piston surface. Figure 4.4 shows the normalized u velocity at the grid line X=-30 mm when the crank is at  $-330^\circ$  bTDC. The u

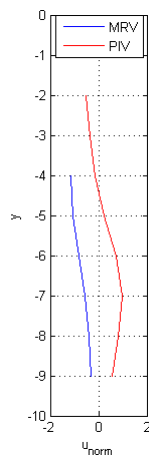


Abbildung 4.4: Normalized u velocity at X=-30 mm; Crank at  $-330^\circ$  bTDC

velocities are almost perfectly correlated, but have opposite directions due to the influence of the piston.

---

### Defining the Directional Correlation Coefficient

---

The purpose of Directional Correlation Coefficient ( $\gamma_D$ ) coefficient is to bring down the value of the correlation coefficient in case of direction reversal of flows. The Directional correlation is found using the following procedure

1. For both the normalized MRV and PIV data, assign the value 1 to a variable (say,  $a$ ) if the normalized velocity at that point is positive or zero. If negative, assign the value -1.
2. Multiply  $a_{\text{MRV}}$  with the corresponding  $a_{\text{PIV}}$ . If both the normalized velocities were of the same sign (flow is in the same direction), the product (say,  $P$ ) would be 1. Else, it would take the value of -1.
3. The fraction of '1's in  $P$  is the Directional Correlation Coefficient,  $\gamma_D$ .

$\gamma_D = 1$  means that at all points along the line, the flow is in the same direction. If  $\gamma_D = 0$ , the flow is in the opposite direction at all points along the line.

---

### The new Correlation Coefficient

---

To account for the direction in the correlation coefficient, the Pearson's correlation coefficient is multiplied with the directional correlation coefficient.

$$\gamma'_{XY} = \gamma_{XY} \cdot \gamma_D \quad (4.5)$$

For the sample data in Table 4.1, this new correlation coefficient is compared to the Pearson's correlation coefficient in the following Table 4.3

	$\gamma_{\text{MRV,PIV}}$	$\gamma'_{\text{MRV,PIV}}$
$u_{\text{norm}}$	0.656	0.562
$v_{\text{norm}}$	0.926	0.926

Tabelle 4.3: Comparison of correlation coefficients

---

#### 4.2.2 Quantitative comparison using Root Mean Square Deviation (RMSD)

---

To quantify the relative deviation between 2 data sets (One being the true values and the other being the test values), a frequently used technique in statistics is the Root mean square deviation (RMSD) [Sclove (2013)]. For a raw data set, RMSD is defined as

$$RMSD, \hat{\sigma}(x) = \sqrt{\frac{\sum_{i=1}^n ((x_t)_i - x_i)^2}{n}} \quad (4.6)$$

where,  $x_t$  are the elements of the true data and  $x$  are the elements of the test data. Here, the PIV data can be considered to be the true data set and MRV data to be the test data set. A higher value signifies a larger deviation of the data from the true value.

The RMSD for the normalized  $u$  and  $v$  velocities from Table 4.2 are  $\hat{\sigma}_u = 0.466$  and  $\hat{\sigma}_v = 0.731$  respectively.

The overall flow field from the MRV data can be considered to be acceptable only if  $\gamma_{\text{MRV,PIV}} > 0.5$  and  $\hat{\sigma} < 1$  for both the normalized velocities.

---

#### 4.2.3 Predicting the region of validity

---

Even if the entire flow field along a grid line might not be acceptable, certain regions in the line taken separately would obey the above conditions. These regions should not be too small, because all flows tend towards perfect correlation as the size of the region tends to zero. The best size would be of the order of magnitude of size of large scale flow features i.e  $\mathcal{O}(10)mm$ . Thus, the data from each section of the grid shown in Figure 4.1 can be used for comparison. For a 2D flow, the flow inside an imaginary rectangular area would behave the same in all situations if the  $u$  and  $v$  velocity distribution on atleast 2 adjacent sides are kept the same; provided that the dimensions of the rectangle are

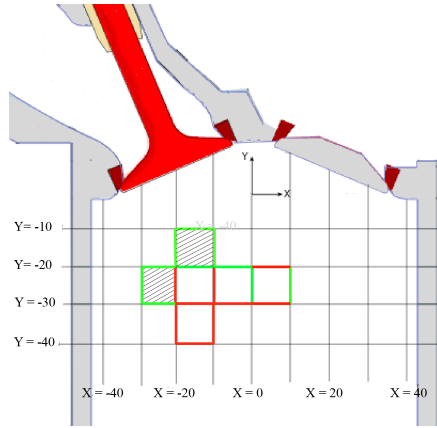


Abbildung 4.5: Green sides represent sections where the acceptability condition is met. Red sides represent regions where it is not. Hatched areas represent region of validity. All dimensions are in *mm*

less than the order of magnitude of size of the significant flow feature in that region.

For more constraint in selection of region of validity, it is proposed that the flow is valid within a smallest closed region of the grid if and only if atleast 3 of the 4 sides satisfy the acceptability condition mentioned in Section 4.2.2. The leniency to allow a region to be valid even though all the sides do not satisfy the acceptability condition has been made because there is always a chance that the data might be erroneous only along a grid line on which the comparison is made but, valid throughout the region inside. The probability of 2 or more sides having such random errors is very less. Figure 4.5 shows a hypothetical case with all the possible outcomes. The hatched areas represent the valid regions.

---

#### 4.2.4 Effects of Compressibility

---

The real engine used to obtain the PIV data uses air as the working fluid, which is compressible. To capture the flow using magnetic resonance ,the model engine uses water which is an incompressible fluid. There are two reasons for compression or expansion of fluid inside the engine

1. Compression due to flow velocities near to sonic speed(Mach number close to 1)
2. Compression or expansion due to the piston

The real engine runs at 800 rpm with an intake pressure of 0.95 bar. The maximum velocity of flow in the engine occurs as the flow exits the valve. The maximum velocity of flow inside this engine from the PIV data in the mid-valve plane is observed to be  $< 25$  m/s throughout the operating cycle. This gives a maximum Mach number of 0.073 which is  $\ll 0.3$ . So the flow can be assumed to be incompressible.

In the real engine, compression of air occurs towards the end of the compression stroke (Piston near TDC)when both the intake and the exhaust valves are fully closed.But, when the piston is at the TDC during the beginning of the intake stroke, the inlet and exhaust valves are slightly open and the pressure is close to the ambient pressure throughout. Any localized high or low pressure would propagate at velocities of the magnitude of speed of sound which is much greater than the flow velocities, thus, equalizing the pressures inside the engine.



---

## 5 Flow through the valve curtain

---

The valve curtain is defined as the annular area between the valve head and the valve seat [Tahry u. a. (1987)]. The flow over the valve curtain is important as it determines the behaviour of flow into the engine cylinder. The behaviour of flow through the valve curtain is analysed as a function of crank angle ( $\alpha$ ) rather than the valve lift because, at a specific valve position, the flow through the valve curtain is different during the forward and the return stroke of the valve.

---

### 5.1 Coordinate system definition

---

The  $\xi$ - $\eta$ - $\zeta$  coordinate system is transformed to a cylindrical coordinate system  $r$ - $\eta$ - $\theta$ , with origin remaining the same.  $r$  is the radial coordinate and  $\theta$  is the angular coordinate.  $\theta$  is positive in the counter-clockwise direction, when the valve is viewed from the top (as shown in Figure 5.1 ). This is similar to the coordinate system defined in Freudenhammer u. a. (2014). The Figure shows a contour plot of the radial velocity,  $U_r$ , on the iso-surface  $r = 15.5\text{mm}$  for  $-180^\circ \leq \theta \leq 180^\circ$ . The unit normal vector to this surface is along the radial direction pointing outwards into the

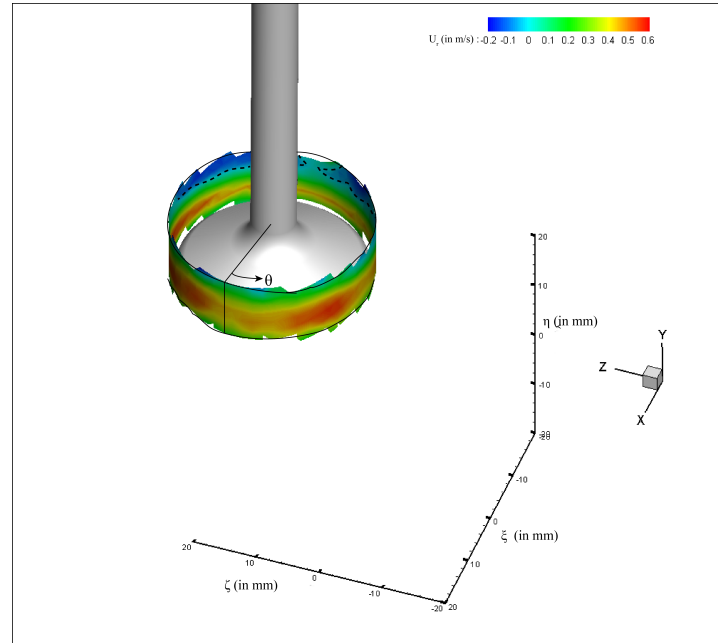


Abbildung 5.1: Valve curtain with iso-surface of radius = 15.5 mm

cylinder. Thus, a positive radial velocity implies an outflow through the valve curtain into the engine cylinder while a negative value implies flow into the valve curtain towards the valves.

---

### 5.2 Evolution of flow through the valve curtain during the intake stroke

---

As mentioned, the intake stroke of the engine begins at crank angle  $\alpha = -390^\circ$  bTDC and ends when the valve returns back to its initial closed position at  $-120^\circ$  bTDC. For brevity of analysis, the development of flow through the valve curtain is divided into 6 different time stages, each lying within a range of crank angles as shown in Table 5.1.

Crank angle, $\alpha$ (in $^{\circ}$ bTDC)	Stage of curtain flow
$-390^{\circ}$ to $-353^{\circ}$ $-139^{\circ}$ to $-120^{\circ}$	Opening and closing stages of valves
$-343^{\circ}$ to $-306^{\circ}$	Uniform outflow
$-297^{\circ}$ to $-270^{\circ}$	Growth of recirculation region
$-260^{\circ}$ to $-222^{\circ}$	Steady outflow with recirculation
$-213^{\circ}$ to $-195^{\circ}$	Decay of recirculation region
$-185^{\circ}$ to $-148^{\circ}$	Reformation of uniform outflow

Tabelle 5.1: Stages of evolution of flow through the valve curtain

### 5.2.1 Recirculation of flows

These recirculation regions are formed due to the presence of a backward step between the inlet port and the walls of the cylinder [Arcoumanis u. Whitelaw (1987)]. The fraction of flow that gets recirculated depends on the Reynolds number. A larger Reynolds number implies larger recirculation. In 3D space, these recirculations form a connected region giving rise to a horse-shoe vortex structure. Consider a control surface representing the valve curtain as shown

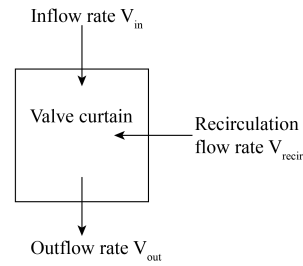


Abbildung 5.2: Schematic of flows through valve curtain

in Figure 5.2.

The net flow into the valve curtain is due to flow from the inlet port (flow rate of  $\dot{V}_{in}$ ) and recirculation (flow rate of  $\dot{V}_{recirc}$ ) from the cylinder. The net outflow through the curtain is  $\dot{V}_{out}$ . By the principle of mass conservation for an incompressible fluid within this control surface,  $\dot{V}_{out} = \text{net influx} = \dot{V}_{in} + \dot{V}_{recirc}$ . Physically, this means that the flow that

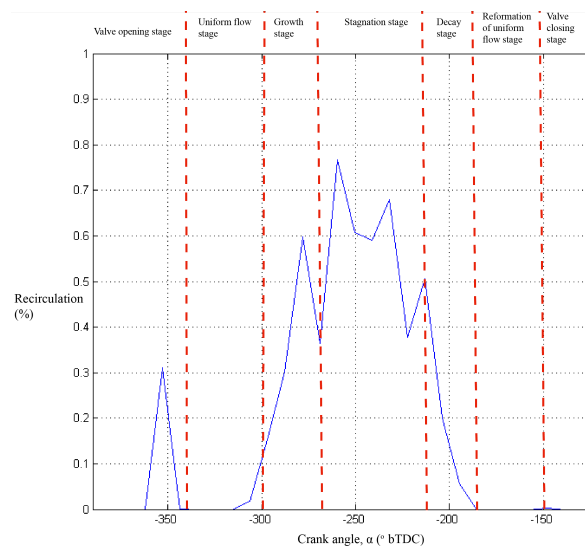


Abbildung 5.3: Percentage recirculation into the valve curtain at various crank positions

gets recirculated is pushed out along with the outflow through the curtain at a different location. The recirculation

thus, does not reduce the net flow into the cylinder. It can be considered as a blockage of flow in that region. The percentage recirculation can be found out from Equation 5.1

$$\text{Percentage recirculation} = \frac{\dot{V}_{recirc}}{\dot{V}_{in}} = \frac{\dot{V}_{recirc}}{\dot{V}_{out} - \dot{V}_{recirc}} \quad (5.1)$$

The percentage recirculation during the intake stroke with the various stages are plotted in Figure 5.3. A typical flow through the valve curtain at  $-270^\circ$  bTDC is shown in Fig 5.1 and the regions of overflow and underflow are marked. It is found that recirculation zones are formed when the valve is at  $\eta < 5\text{mm}$ . It is also observed that the recirculated fluid has a velocity of around  $0.1\text{ m/s}$  in the  $\theta$  direction between  $-90^\circ \leq \theta \leq 90^\circ$ .

### 5.2.2 Stage 1: Opening and closing stages of the valves

The data during the opening stages are not valid as the MRV and the PIV flow data within the engine do not resemble and their magnitudes deviate a lot, due to the presence of the piston. During the closing stages of the valves, there is an unusually large amount of recirculation between  $60^\circ \leq \theta \leq 120^\circ$ . This information has to be validated before conclusions can be drawn.

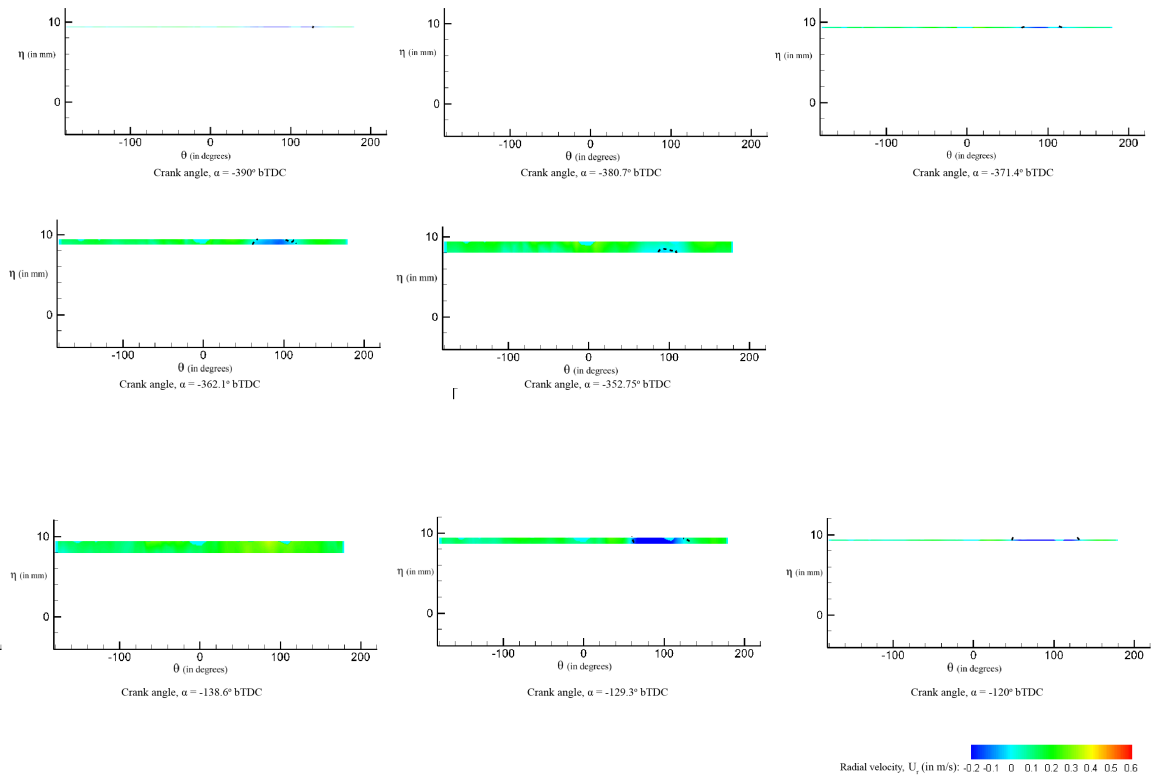


Abbildung 5.4: 2D projection of flow through the valve curtain in the opening and closing stages

### 5.2.3 Stage 2: Uniform outflow ( $-343^\circ \text{ bTDC} \leq \alpha \leq -306^\circ \text{ bTDC}$ )

Between  $-343^\circ \text{ bTDC}$  and  $-306^\circ \text{ bTDC}$  the flow through the valve curtain is largely uniform. The flow velocities are small and there is no recirculation of the flows. The MRV data does not match well with the PIV data within the cylinder, because of flow reversal due to the presence of the piston. The flow through the valve curtain is not significantly influenced by the presence of the solid boundary of the piston and hence, is assumed to be valid very close to the valves. Figure 5.4 shows the representation of a valve curtain, when viewed in the direction of the axis of the valve. It is divided into 5 sections viz.  $-20^\circ \leq \theta \leq 20^\circ$ ,  $-90^\circ \leq \theta \leq -20^\circ$ ,  $20^\circ \leq \theta \leq 90^\circ$ ,  $-180^\circ \leq \theta \leq -90^\circ$ , and  $90^\circ \leq \theta \leq 180^\circ$  based on the similarity in behaviour of flows in each section. The average percentage of inflow entering the engine cylinder through the valve curtain in this stage is also shown. The percentage per unit  $\theta$  for each section is shown in brackets.

It can be observed that the percentage of outflow per unit  $\theta$  are approximately the same in all sections, implying uniform flow throughout the curtain. There is no recirculation of flow into any zone.

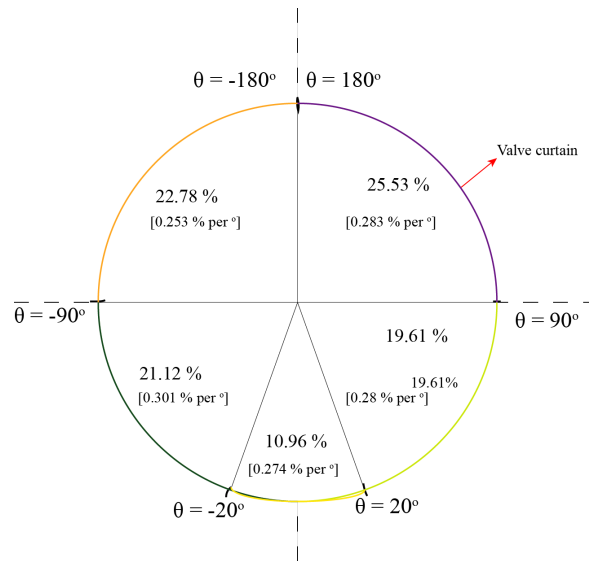


Abbildung 5.5: Division of valve curtain into sections. Average percentage flow through each section is also shown. The average percentage per unit  $\theta(^{\circ})$  is shown in brackets.

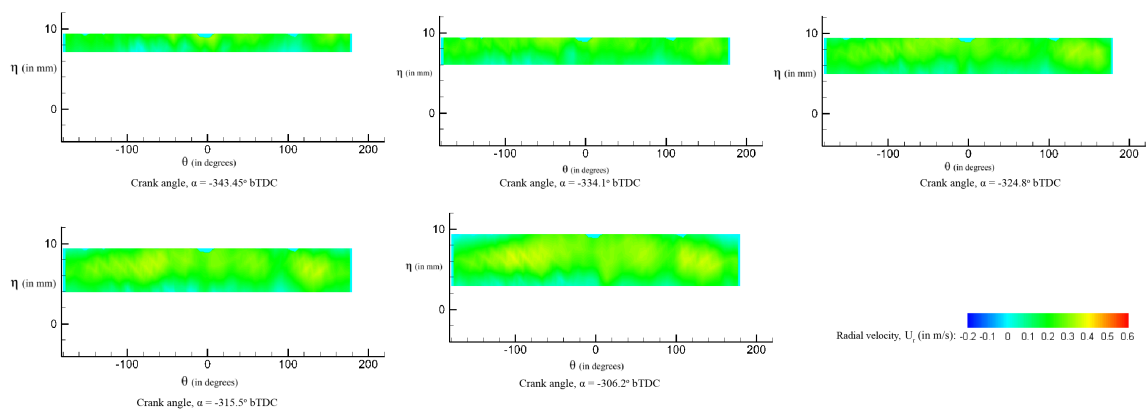


Abbildung 5.6: 2D projection of flow through the valve curtain in the uniform flow stage

### 5.2.4 Stage 3: Growth of Recirculation region ( $-297^\circ \text{ bTDC} \leq \alpha \leq -270^\circ \text{ bTDC}$ )

Between crank locations of  $-297^\circ \text{ bTDC}$  to  $-270^\circ \text{ bTDC}$ , recirculation regions start to form and grow behind the valves (between  $-180^\circ \leq \theta \leq -90^\circ$  and  $90^\circ \leq \theta \leq 180^\circ$ ) as shown by dotted region in Figure 5.8. They start forming from  $\theta = \pm 180^\circ$  and grow towards the sides of the valves ( $\theta = \pm 90^\circ$ ). Since the flow rates through the valve curtain increases with increase in the crank angle, the radial velocity increases and hence, strength of recirculation increases. In this stage, formation and growth of vortices on the valve stem are observed. These vortices push the fluid away from  $-20^\circ \leq \theta \leq 20^\circ$  region of the valve which reduces the flow in that region and thereby increases the flow through the sides ( $-90^\circ \leq \theta \leq -20^\circ$  and  $20^\circ \leq \theta \leq 90^\circ$ ). This is the reason for the formation of dumbbell/Moustache shaped high velocity field in the overflow region of the curtain.

Behind the valves, the recirculation of flow increases from 0.6 % to 2 % of the net outflow in that region during this stage. The percentage of flow recirculated in this region at different crank angle positions are tabulated in Table 5.2. The maximum recirculating velocity is 26% of the mean inflow velocity.

Crank angle, $\alpha$ (in $^\circ \text{ bTDC}$ )	%Recirculation
$-297^\circ$	0.634
$-287.6^\circ$	1.12
$-278.3^\circ$	2.02
$-269^\circ$	1.89

Tabelle 5.2: %Recirculation behind the valve at different crank position

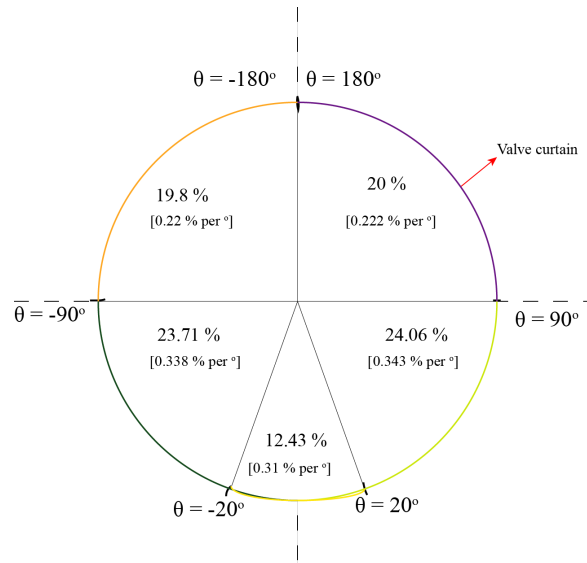


Abbildung 5.7: Average percentage outflow through the different sections of the valve during Growth stage. The average percentage per unit  $\theta(^\circ)$  is shown in brackets.

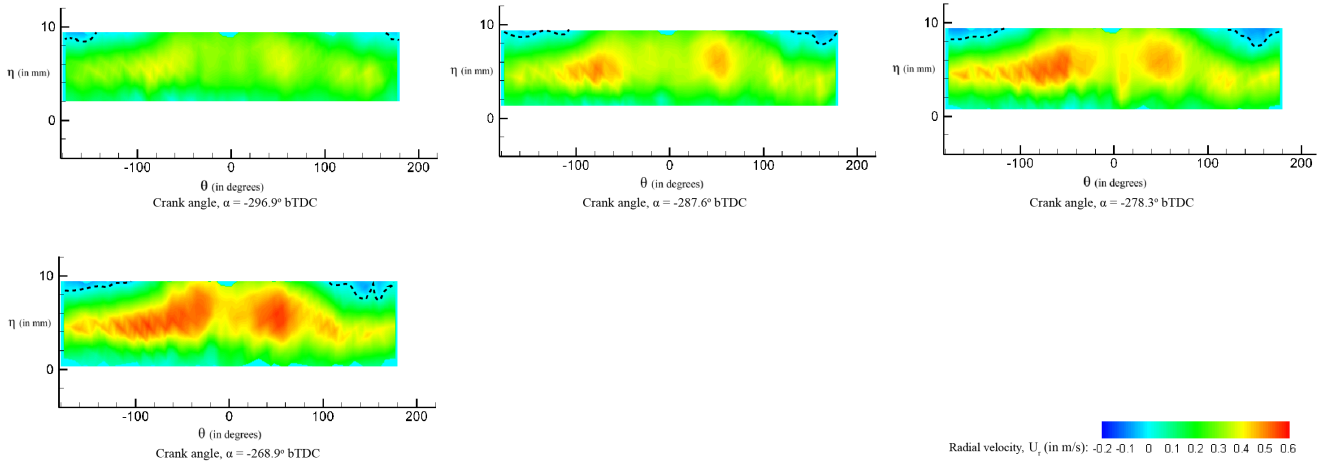


Abbildung 5.8: 2D projection of flow through the valve curtain in the growth of recirculation region stage

The magnitude of outflow through  $60^\circ \leq \theta \leq 100^\circ$  is more than  $-100^\circ \leq \theta \leq -60^\circ$  by an average of 6%. This difference is possibly due to flow from the adjacent valve on one side and the presence of wall on the other. The latter has a higher back pressure.

#### 5.2.5 Stage 4: Stagnation of Recirculation region ( $-260^\circ \text{ bTDC} \leq \alpha \leq -222^\circ \text{ bTDC}$ )

The valves are almost fully open and stationary in this stage. The deceleration of the piston is small and so, the inflow is almost uniform. Due to this quasi-steady nature of the valves and the inflow, there is not much change in the location, size and strength of the recirculation region. The recirculation rates behind the valves maintain an average of 2% of the outflow behind the valves. The flow through the back of the valves reduce by 5 % due to the increase in recirculation. The flow through the sides of the valve curtain (per unit  $\theta(^\circ)$ ) is 20% more than the flow through the front due to the valve stem vortices. It can be observed from the deviation of streamlines of flow over the valves towards the sides as shown in Figure 5.9 . This is the reason for the formation of Moustache or dumbbell shaped regions of higher radial velocities through the curtain.

The recirculation of flow has an average of approximately 0.8 % of the net inflow. But, the negative  $\theta$  half ( $-180^\circ \leq$

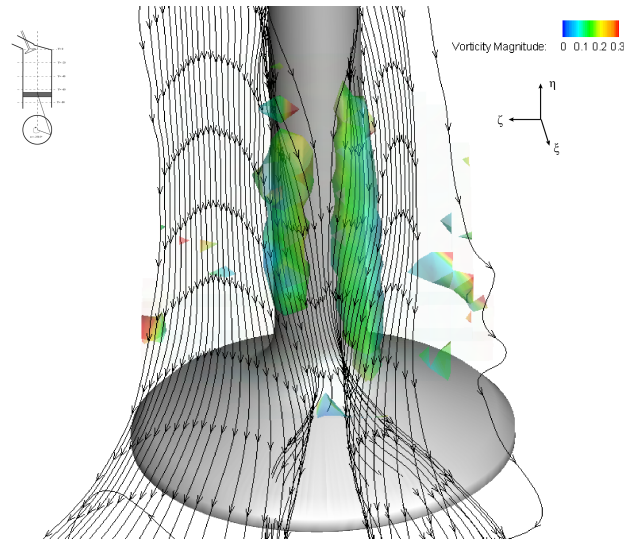


Abbildung 5.9: Redirection of streamlines on the valves due to valve stem vortices

$\theta \leq -90^\circ$ ) has 15% more recirculation than the positive half due to the absence of flow from the adjacent valve. The maximum recirculating velocity is  $\approx 30\%$  of the mean inflow velocity. The percentage of flow recirculated in this region at different crank angle positions are tabulated in Table 5.3.

Crank angle, $\alpha$ (in $^{\circ}$ bTDC)	%Recirculation
$-259.6^{\circ}$	2.1
$-250.3^{\circ}$	1.97
$-241^{\circ}$	1.98
$-231.7^{\circ}$	2.4
$-222.4^{\circ}$	1.98

Tabelle 5.3: Percentage recirculation behind the valve at various crank angles

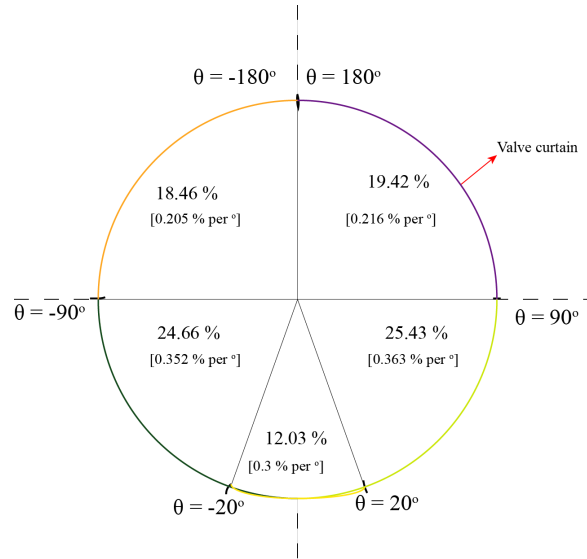


Abbildung 5.10: Average percentage outflow through the different sections of the valve during Stagnation stage. The average percentage per unit  $\theta(^{\circ})$  is shown in brackets.

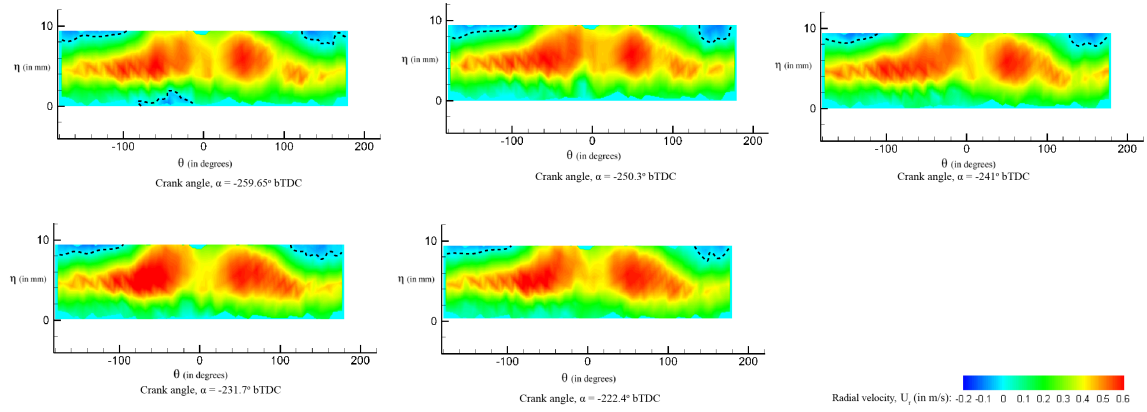


Abbildung 5.11: 2D projection of flow through the valve curtain in the Stagnation of recirculation region stage

### 5.2.6 Stage 5: Decay of Recirculation region ( $-213^\circ \text{ bTDC} \leq \alpha \leq -185^\circ \text{ bTDC}$ )

The size of the recirculation region decreases both in  $\eta$  and  $\theta$  directions. It shrinks from a maximum of  $\eta \approx 7\text{mm}$  and  $-180^\circ \leq \theta \leq -90^\circ$  at  $\alpha = -213^\circ \text{ bTDC}$  to  $\eta \approx 9.2\text{mm}$  at and  $-180^\circ \leq \theta \leq -125^\circ$  at  $\alpha = -194.5^\circ \text{ bTDC}$ . The magnitude of maximum inflow recirculation velocities in the region also drops by around 33%. Behind the valves, the recirculation of flow decreases from 1.8% to 0.3% of the outflow in that region during this stage. The net recirculation reduces from 0.5% to almost zero. The presence of a comparatively stronger recirculation region in  $-180^\circ \leq \theta \leq -90^\circ$  ( $\approx 1.5$  times) redirects more flow towards the positive half. The Moustache shaped flow field through the sides of the valve curtain is highly symmetric and (per unit  $\theta$ ) is more prominent (25% more than the flow through the front) and as the vortex cores on the valve stem have higher strength during these crank positions. The maximum recirculating velocity is 18% of the mean inflow velocity. The percentage of flow recirculated behind the valves at different crank angle positions are tabulated in Table 5.4.

Crank angle, $\alpha$ (in $^\circ \text{ bTDC}$ )	%Recirculation
$-213.1^\circ$	1.8
$-203.8^\circ$	0.82
$-194.5^\circ$	0.3

Tabelle 5.4: Percentage recirculation behind the valve at various crank angles



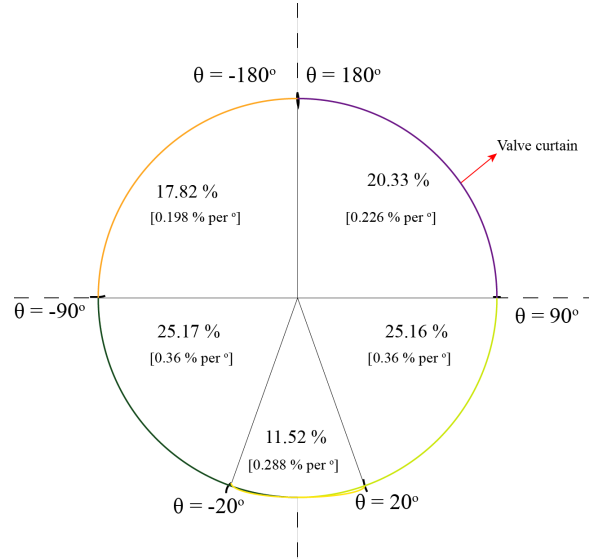


Abbildung 5.12: Average percentage outflow through the different sections of the valve during Decay stage. The average percentage per unit  $\theta(^{\circ})$  is shown in brackets.

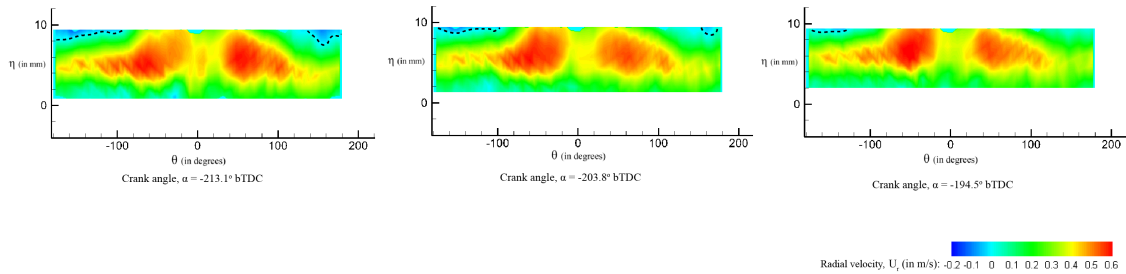


Abbildung 5.13: 2D projection of flow through the valve curtain in the decay of recirculation region stage

---

### 5.2.7 Stage 6: Re-formation of uniform flow region ( $-176^\circ \text{ bTDC} \leq \alpha \leq -148^\circ \text{ bTDC}$ )

---

In this stage, the valve moves up quickly and the flow rate into the cylinder decreases as the piston is close to its BDC position. From the MRV data, it can be observed that the outflow becomes uniform through the valve curtain again. But this information cannot be considered as true because the MRV data within the engine is not found to be valid in comparison to the PIV data.

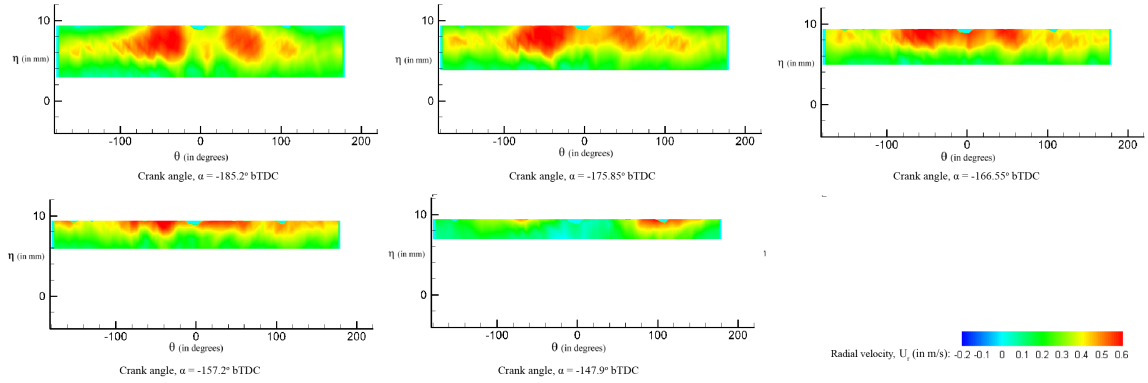


Abbildung 5.14: 2D projection of flow through the valve curtain in the reformation of uniform flow stage

---

## 6 Analysis of vortex structures from MRV data

---

### 6.1 Identification of vortex cores

---

Vortices are an important flow feature as it determines the mixing of fuel and air inside the engine. They are also responsible for recirculation and redirection of flows into or away from the cylinder.

The requirements for a vortex core are [Hussain u. Jeong (1995)]

1. A vortex core must have net vorticity.
2. The geometry of the identified core must be Galilean invariant.

Presence of a local pressure minimum at the core is valid only for 2D vortex cores. A pressure minimum can occur in unsteady irrotational motion too. Presence of vorticity is also not a sufficient condition as shear flows near the walls of the engine will have a non-zero vorticity. Pathlines and streamlines are not Galilean invariants and hence, cannot be used to extract a 3D vortex cores. The popular methods are Q-criteria and  $\Delta$  criteria. Q-criteria being more restrictive, is used here to extract vortex cores from the 3D MRV data.

---

#### 6.1.1 The Q-criteria

---

'Q' is defined as the second invariant of the velocity gradient tensor ( $\bar{\bar{G}}$ ). It represents the local balance between the vorticity magnitude and the shear strain rate. [Hussain u. Jeong (1995)]

$$G_{ij} = \begin{pmatrix} \frac{\partial u}{\partial x} & \frac{\partial u}{\partial y} & \frac{\partial u}{\partial z} \\ \frac{\partial v}{\partial x} & \frac{\partial v}{\partial y} & \frac{\partial v}{\partial z} \\ \frac{\partial w}{\partial x} & \frac{\partial w}{\partial y} & \frac{\partial w}{\partial z} \end{pmatrix} = \frac{\partial u_i}{\partial x_j} \quad (6.1)$$

This tensor matrix can be decomposed into a symmetric ( $S_{ij}$ ) and a skew-symmetric ( $\Omega_{ij}$ ) matrix with  $S_{ij} = \frac{1}{2} \cdot (\frac{\partial u_i}{\partial x_j} + \frac{\partial u_j}{\partial x_i})$  and  $\Omega_{ij} = \frac{1}{2} \cdot (\frac{\partial u_i}{\partial x_j} - \frac{\partial u_j}{\partial x_i})$ .  $S_{ij}$  is the Strain Rate tensor and  $\Omega_{ij}$  is the Vorticity tensor.

The second invariant of velocity gradient tensor is

$$Q = \frac{1}{2} \cdot (tr(\bar{\bar{G}})^2 - tr(\bar{\bar{G}}^2)) = \frac{1}{2} \cdot (||\bar{\bar{\Omega}}||^2 - ||\bar{\bar{S}}||^2) \quad (6.2)$$

A vortex is proposed to exist if the vorticity magnitude overcomes the strain rate i.e  $Q > 0$  i.e it is a connected region of fluid with second invariant of  $\nabla \bar{u} > 0$  [Hussain u. Jeong (1995)]. This is a necessary, but not sufficient condition to prove the existence of a vortex core. An additional requirement is the necessity of pressure being lower than the ambient value. The pressure gradients in the MRV velocity field data are found out from the Navier-Stokes equations at the locations where  $Q > 0$ . A positive pressure gradient towards a lower value of  $Q (< 0)$  would imply a local pressure lower than the ambient.

---

#### 6.1.2 Kinematic vorticity number, $N_k$

---

The Kinematic vorticity number,  $N_k$  was introduced to measure the 'quality' of rotation. It is defined as

$$\text{Kinematic vorticity number, } N_k = \frac{||\bar{\bar{\Omega}}||}{||\bar{\bar{S}}||} = \sqrt{1 + \frac{2Q}{S_{ij} \cdot S_{ij}}} \quad (6.3)$$

It is a point wise measure of the vorticity magnitude, non-dimensionality by the norm of the strain rate. Since it is a non-dimensional number, it does not provide the strength of the vortex.  $N_k = \infty$  represents solid body rotation while  $N_k = 0$  corresponds to irrotational motion. Closer the value of  $N_k$  to 0, the more irrotational the vortex is.  $N_k > 1$  also implies  $Q > 0$ . Core of an axisymmetric vortex column is a maximally connected spatial region with  $N_k > 1$  [Hussain u. Jeong (1995)].

---

## 6.2 Major vortex cores that have been identified from MRV data

---

Since an entire 3D data of the velocity flow field over time is available from MRV, the velocity gradient tensor ( $\bar{\bar{G}}$ ) at all spatial locations and at each phase angle can be computed easily. From this data, the values of  $Q$  and  $N_k$  are computed. Pressure gradients at each point can be computed from the N-S equations. A contour plot (in 2D for mid-valve, tumble and cross-tumble planes) of  $Q$  is made and the regions where  $Q > 0$  and pressure gradient (in the direction of decreasing  $Q$ )  $> 0$  are identified as vortex cores. In almost all cases, pressure gradient criterion has been satisfied when  $Q > 0$ . The Figure 6.1 shows locations of vortex cores identified using the  $Q$  criteria in the mid-valve plane. For understanding the structure and behaviour of the cores, iso-surfaces of constant  $Q$  are displayed. These iso-surfaces represent regions within which the vortex core line lies. A higher value of  $Q$  would imply more dominance of vorticity over strain rate which is observed towards the core. So, an iso-surface with a large value of  $Q$  would imply a stronger vortex core in that region.

Using the above mentioned methods, 3 major vortex structures have been identified inside the engine

1. Toroid vortices underneath the valves.
2. Horse-shoe vortex over the valves and into the engine cylinder.
3. Bluff body vortices in front of the valve stem. (valve stem vortices)

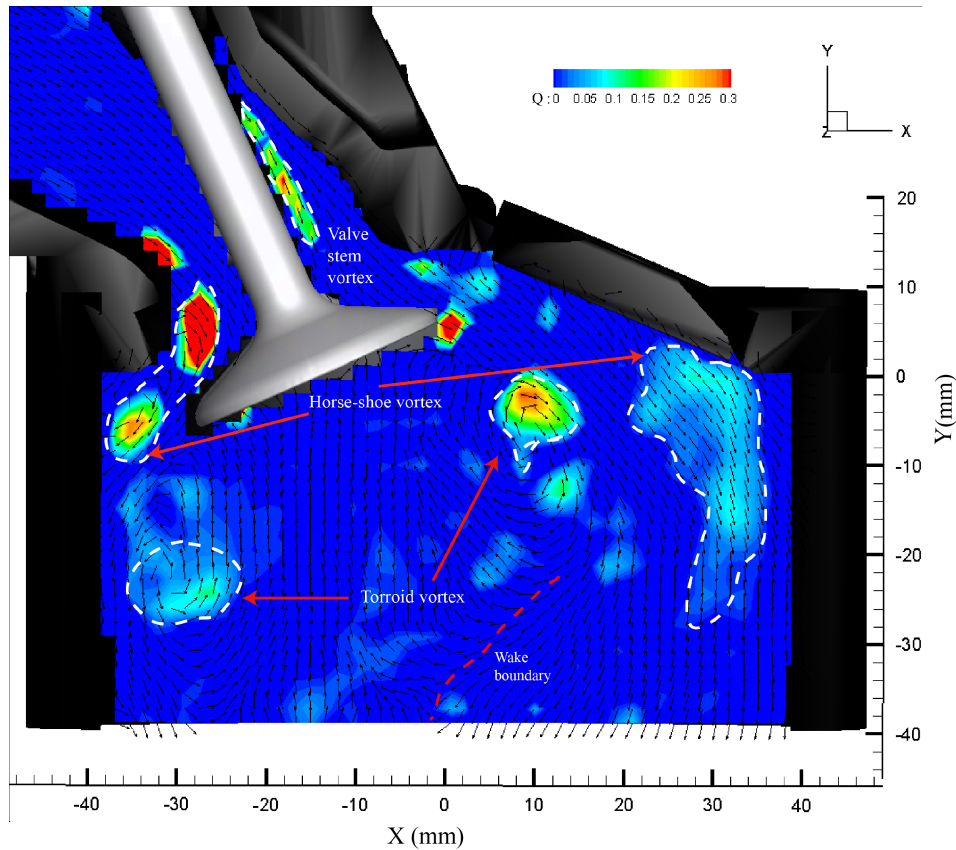


Abbildung 6.1: Vortex cores located in mid-valve plane

All the vortices have been found to exist within the valid regions of MRV data, where influence of the piston is negligible.

---

### 6.2.1 Toroid vortices

---

Toroid vortices are commonly observed during flow over a bluff body; in this case, a valve head. It occurs due to the separation of flow as it leaves the edge of the valves.

The shape of the toroid vortices is captured at planes of constant  $Y$  using the  $Q$  criteria. The vortices form a closed circular loop in the  $\xi\zeta$  plane, but appears elliptical in the  $XZ$  plane as shown in Figure 6.2. The percentage of flow recirculated by the toroid vortices were analysed at  $Y = -10\text{mm}$ .

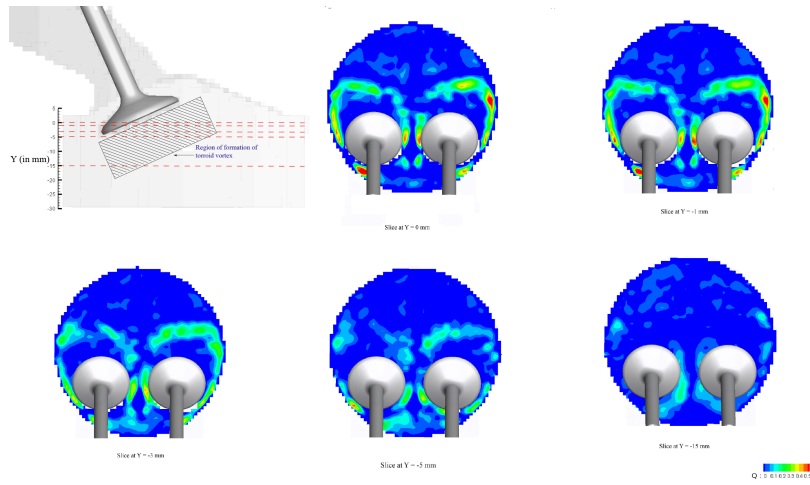


Abbildung 6.2: Contour plot of  $Q$  at crank angle  $-250^\circ$  bTDC representing the closed core of Toroid vortices at different XZ-planes

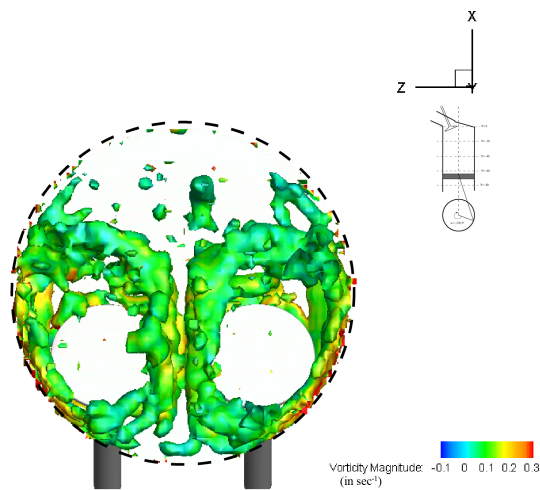


Abbildung 6.3: Iso-surface of  $Q = 0.05$  at crank angle  $-269^\circ$  bTDC representing the core of Toroid vortices when viewed from the bottom of the engine cylinder. Vorticity magnitude is shown in  $\text{sec}^{-1}$

---

### 6.2.2 Horse-Shoe vortices

---

These vortices originate from the flow reversal at the back of the valves ( $\theta = \pm 180^\circ$ ). During the growth stage of the recirculation region, the vortex extends towards  $\theta = \pm 90^\circ$ . Propelled by the comparatively higher velocity flows from the sides of the valve, the swirling fluid flows along the walls of the cylinder till it impinges with a similar flow from the other half. This pushes the swirling fluid down, forming the tail of the horse-shoe vortex. Horse-shoe vortices are observed in the valid MRV data between crank angles of  $-278^\circ \text{ bTDC} \leq \alpha \leq -176^\circ \text{ bTDC}$  with a maximum size and strength between  $-232^\circ \text{ bTDC} \leq \alpha \leq -194.5^\circ \text{ bTDC}$ . Figure 6.4 shows the iso-surface of  $Q$  used to capture the Horse-shoe vortex cores at  $\alpha = 250^\circ \text{ bTDC}$ .

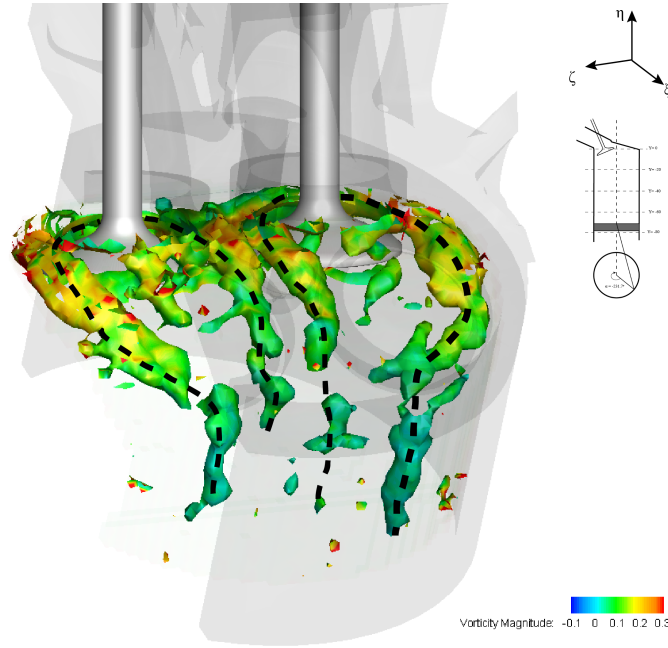


Abbildung 6.4: Iso-surface of  $Q = 0.1$  at crank angle  $-232^\circ \text{ bTDC}$  representing the core of Horse-shoe vortex . Vorticity magnitude is shown in  $\text{sec}^{-1}$

These vortices observed from the MRV data seem to originate and develop over the valve head rather than under it, as predicted by Koehler u. a. (2014).

---

### 6.2.3 Valve stem vortices

---

The flow impinges the cylindrical valve stem at an angle. Bluff body vortices are hence formed behind the valve stem. These vortices are termed as valve-stem vortices. They divert  $\approx 20\%$  more flow from the front towards the sides of the valve, thus, strengthening the Horse-shoe vortex in these regions. Figure 6.5 shows the iso-surface of  $Q$  used to capture the vortex core above the valves at  $\alpha = 250^\circ \text{ bTDC}$ .

---

## 6.3 Kinematic vorticity number

---

It is found that for all 3 types of vortices inside the engine, the Kinematic vorticity number,  $1 \leq N_k \leq 2.5$ . This low value implies that the vortices have a more irrotational behaviour.

---

## 6.4 Measuring region of influence of the vortices

---

The vortices influence the mixing of fuel and air in the engine by creating regions of uneven concentrations which would affect overall performance and efficiency. It is hence very crucial to identify the region within which these vortices influence the flow. The toroid and the valve-stem vortices are basically bluff body vortices and their influence is within the wake region. The following region of influence of the vortices is measured for an inflow Reynolds number of 20000.

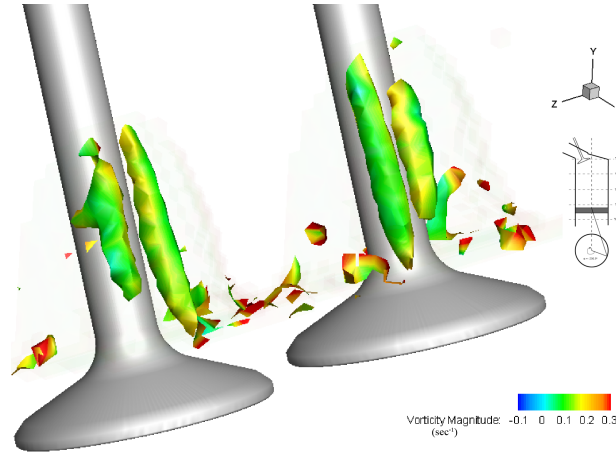


Abbildung 6.5: Iso-surface of  $Q = 0.1$  at crank angle  $-250^\circ$  bTDC representing the core of valve stem vortex . Vorticity magnitude is shown in  $\text{sec}^{-1}$

#### 6.4.1 Toroid vortices

Approximating the wake as a circular region in the mid-valve plane, its diameter would be an appropriate measure of the region of influence. The boundary of the wake is obtained by a Lagrangian method. To identify the wake region in the mid valve plane, the flow field is sampled every 1 mm along a constant X line underneath the valves. The position of the particles at the next instant is calculated based on the flow properties at the current time step. If two adjacent particles show significant deviation compared to others in a free wake, it shows that the particles are on either side of the wake boundary. The average region of influence (diameter of the wake) of the toroid vortices in the valid region ( $-280^\circ \text{ bTDC} \leq \alpha \leq -150^\circ \text{ bTDC}$ ) of the mid-valve plane is found to be  $\approx 40\text{mm}$  from the valve head, along the valve axis. In the cross-tumble plane, the toroid vortices influence upto  $\frac{3}{4}$ th of the cylinder diameter as observed in Figure 6.2.

#### 6.4.2 Horse-shoe vortices

To find the region of influence of the horse-shoe vortex, iso-surfaces are made with  $Q = 0$ . The region of  $Q > 0$  are uninfluenced by the vortex. The diameter of this iso-surface is considered to be the region of influence. For a typical horse shoe vortex at  $\alpha = -250^\circ$  bTDC, the region of influence varies from a diameter of  $10\text{mm}$  in the back of the valves to around  $15\text{mm}$  well inside the engine. In the mid valve plane, the depth of influence is maximum and is approximately till  $Y = -30\text{mm}$ .

#### 6.4.3 Valve-stem vortices

The valve stem vortices are strong and localized. Size of region of influence is considered to be the average diameter of the iso-surface  $Q = 0$  on the valve stem. For a valve-stem vortex at  $\alpha = -250^\circ$  bTDC, the region of influence is  $\approx 3\text{mm}$  diameter from the valve-stem and  $25\text{mm}$  long.

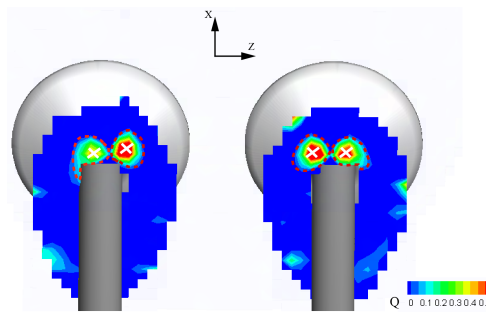


Abbildung 6.6: Contour plot of  $Q$  at crank angle  $-250^\circ$  bTDC representing the core of valve stem vortex.

---

## Literaturverzeichnis

---

- [Arcoumanis u. Whitelaw 1987] Arcoumanis, C. ; Whitelaw, J.H.: Fluid mechanics of internal combustion engine - a review. In: Journal of Mechanical Engineering Science (1987)
- [Bansal u. Brar 2005] Bansal, R.K. ; Brar, J.S.: A textbook of Theory of machines. Laxmi publications, 2005
- [Elkin u. Alley 2007] Elkin, C.J. ; Alley, M.T.: Magnetic resonance velocimetry: Applications of magnetic resonance imaging in measurement of fluid motion. In: Exp Fluids (2007)
- [Frayne u. a. 1995] Frayne, R ; Steinman, D. A. ; Rutt, B. K. ; Ethier, C. R.: Accuracy of MR phase contrast velocity measurements for unsteady flow. In: Journal of Magnetic Resonance Imaging 5(4) (1995), S. 428–431
- [Freudenhammer u. a. 2014] Freudenhammer, D. ; Baum, E. ; Peterson, B. ; Böhm, B. ; Jung, B. ; Grundmann, S.: Volumetric intake flow measurement of an IC engine using magnetic resonance velocimetry. In: Exp. Fluids (2014)
- [Hendrix 2003] Hendrix, A.: Magnets, Spins and Resonances. 2003
- [Hendrix 2004] Hendrix, A.: Magnets, Flow, and Artifacts. 2004
- [Hussain u. Jeong 1995] Hussain, F. ; Jeong, J.: On identification of a vortex. In: Journal of Fluid Mechanics (1995)
- [Koehler u. a. 2014] Koehler, M. ; Hess, D. ; Kratzsch, C. ; Brücker, C.: Flying PIV measurements in a driven IC engine flow. In: 17th International symposium on Applications of Laser techniques to FLuid Mechanics, Lisbon, Portugal, 2014
- [Rieß 2014] Rieß, Sebastian: Entwicklung eines experimentellen Aufbaus zur Erzeugung periodischer Einstromvorgänge innerhalb eines MRT, Technische Universität Darmstadt, Diplomarbeit, 2014
- [Ross 2010] Ross, Sheldon M.: Introductory Statistics. Third Edition. Elsevier, 2010
- [Sclove 2013] Sclove, Stanley L.: A course on statistics for finance. First Edition. CRC press, 2013
- [Tahry u. a. 1987] Tahry, S. E. ; Khalighi, B. ; Kuziak: Unsteady-Flow Velocity Measurements Around an Intake Valve of a Reciprocating Engine. In: SAE Technical Paper (1987)
- [Taylor 1951] Taylor, G.I.: Analysis of the swimming of microscopic organisms. In: Proceedings - The Royal Society (1951)